A&A 492, 3–22 (2008)
DOI: 10.1051/0004-6361:20077621

Astronomy & Astrophysics

Extremely massive young clusters in NGC 1365

E. Galliano[1,2,3], D. Alloin[3,4], E. Pantin[4], G. L. Granato[5], P. Delva[3], L. Silva[6], P. O. Lagage[4], and P. Panuzzo[4,5]

[1] Observatório Nacional, Rua General José Cristino 77, 20921-400 São Cristovão, Rio de Janeiro, Brazil
e-mail: `egallian@on.br`
[2] Departamento de Astronomia, Universidad de Chile, Casilla 36-D, Santiago, Chile
[3] European Southern Observatory, Casilla 19001, Santiago 19, Chile
[4] Laboratoire AIM, CEA/DSM-CNRS-Université Paris Diderot, IRFU/Service d'Astrophysique, Bât. 709, CEA/Saclay, 91191 Gif-sur-Yvette Cedex, France
[5] INAF – Osservatorio Astronomico di Padova, Vicolo Osservatorio 5, 35122 Padova, Italy
[6] INAF – Osservatorio Astronomico di Trieste, via Tiepolo 11, 34131 Trieste, Italy

Received 9 April 2007 / Accepted 20 July 2008

ABSTRACT

Context. In a previous work, three bright mid-infrared/radio sources were discovered in the nuclear region of starburst/AGN galaxy NGC 1365.

Aims. The present study aims to confirm that these sources are indeed young and massive "embedded" clusters, and derive their physical parameters, such as extinction, age and mass.

Methods. Using ISAAC and VISIR at the VLT we obtained maps and low resolution spectra in the near- and mid-infrared. The resulting datasets are first interpreted by comparing the observations with images and spectra of the close-by young cluster R136 in the Large Magellanic Cloud and then by using model predictions for both the nebular emission lines and the spectral energy distribution of the sources.

Results. We produce maps of the region containing the three sources in the R, J, Ks, L' bands and at 12.8 μm and perform their accurate relative positioning. We also provide spectra in the ranges 1.8−2.4 μm, 3.3−4.0 μm, 8.1−9.3 μm and 10.4−13.2 μm. The spectral energy distribution of the three sources rises with wavelength. Emission lines from ionised hydrogen and molecular hydrogen are detected, as well as PAH emission. A conspicuous [NeII] 12.8 μm line is also observed, while neither the [ArIII] 8.9 μm nor the [SIV] 10.4 μm lines are detected. This provides a stringent constraint on the age of the sources: we argue that they are relatively evolved young clusters (6−8 Myr). Owing to their ionising photon emission rates and ages, they must be extremely massive clusters (of the order of 10^7 $M_\odot$). Their mid-infrared spectral energy distribution suggests the presence of two components: (1) an optically thin component, with a continuum comparable to that of R136; and (2) an optically thick component which might be related to subsequent or on-going episodes of star formation. We anticipate that these sources are good candidates for evolution according to a bi-modal hydrodynamical regime, in which matter is trapped at the centre of a compact and massive cluster and generates further star formation.

Key words. ISM: dust, extinction – ISM: HII regions – galaxies: star clusters – galaxies: individual: NGC 1365 – infrared: galaxies

1. Introduction

Starburst regions in close-by galaxies were first resolved in a population of star clusters in the early nineties, thanks to the high angular resolution of the Hubble Space Telescope. The first galaxy-target, NGC 1275 (Holtzman et al. 1992), showed a population of young and massive compact clusters. Soon after, similar objects were encountered in a wide variety of environments, such as dwarf galaxies (O'Connell et al. 1994; Hunter et al. 1994; O'Connell et al. 1995; Leitherer et al. 1996; Gorjian 1996), interacting galaxies (Whitmore et al. 1993; Conti & Vacca 1994; Shaya et al. 1994; Whitmore & Schweizer 1995; Meurer 1995) and circumnuclear star-forming rings (Benedict et al. 1993; Barth et al. 1995; Bower & Wilson 1995; Maoz et al. 1996). Their possible parental link with classical and well-studied globular clusters was proposed and, in subsequent studies, these young massive clusters (abbreviated YMCs) became increasingly referred to as objects likely to evolve into globular clusters after a few Gyrs. Their masses are greater than 10^5 $M_\odot$, with radii smaller than 5 pc and ages below 100 Myr. In the literature, the term super star cluster (SSC) is often associated with YMCs which are bright in the visible, hence suffer little extinction. We prefer to use the generic term YMC in all cases, and specify, whenever needed, whether the YMC is still dust embedded (embedded YMC) or naked (UV-bright YMC).

The youngest YMCs discovered so far may be younger than 1 Myr, and show up as heavily dust-embedded HII regions. Examples of such extragalactic embedded YMCs known to date are still scarce: some were found and discussed in the Antennae galaxies NGC 4038/39 (Mirabel et al. 1998; Gilbert et al. 2000), in Henize 2-10 (Kobulnicky & Johnson 1999), in NGC 5253 (Gorjian et al. 2001), in SBS 0335-052 (Plante & Sauvage 2002), in IIZw40 (Beck et al. 2002), in NGC 1365 and NGC 1808 (Galliano et al. 2005; Galliano & Alloin 2008), in NGC 7582 (Wold & Galliano 2006).

As proposed in Johnson (2004), parallel evolutionary sequences can be imagined for the formation of massive stars and for the formation of massive clusters. Both types of objects start as HII regions deeply embedded in a dust cocoon. In the case of a massive star, this stage is known as the ultra compact HII region (UCHII region) and in the case of a YMC as the ultra dense HII region (UDHII region) (Kobulnicky & Johnson 1999). They are both inconspicuous in the visible and near-infrared (NIR), while bright in the mid-infrared (MIR) and far-infrared (FIR).

Article published by EDP Sciences

They are also intense sources of thermal radio continuum as well as of line emission from ionised gas. The embedding material eventually dissipates and they become detectable as UV-bright sources. The extent to which this parallel is sustainable remains an open question: similarities and differences along the two sequences might bring clues about the conditions for star formation in galaxies, and in particular for the formation of massive star clusters and globular clusters.

We present in this paper the first step of a thorough analysis and modelling of embedded YMCs in nearby spiral galaxies. The three YMCs we are interested in here are located in the starburst circumnuclear region of the Seyfert2 galaxy NGC 1365 (distance 18.6 Mpc, hence 1″ corresponds to 90 pc). Galliano et al. (2005) discovered these sources in the MIR and demonstrated that they coincide with bright thermal centimetre radio sources detected by Sandqvist et al. (1995). They have also been recently detected in the CO molecule by Sakamoto et al. (2007). These authors infer a mass of molecular material of the order of $10^9\ M_\odot$ in the central 2 kpc diameter region, which includes the three YMCs under discussion.

In Galliano et al. (2005), their ages were roughly estimated from their radio spectral indexes and found to be of a few (3) Myr. Accordingly, their masses were estimated to be of the order of $10^6\ M_\odot$.

These clusters are located at the inner Linblad resonance (ILR) in their host galaxy, and also within around 1 kpc from its active galactic nucleus (AGN). Their environment has a slightly above solar metallicity, as expected from the observed metallicity gradient in the disc of NGC 1365 discussed by e.g. Dors & Copetti (2005).

The questions to be addressed in the current paper remain basic ones. What are the spectral characteristics of such YMCs? Are NIR and/or MIR data sufficient for a reliable insight into the properties of embedded YMCs? Do we miss a substantial part of the phenomenon by observing only in the NIR? Which physical parameters can be safely derived for these objects, either in a direct way or through a comparison with models?

The paper is structured as follows: the first part is devoted to the presentation and discussion of the data, while subsequent sections deal with the physical interpretation of the sources. In Sect. 2.1, we describe the acquisition and reduction of the dataset, which consists of NIR/MIR images and spectra, all collected at the ESO/VLT using the instruments ISAAC and VISIR. We first discuss the images and perform the relative registration of the maps at different wavelengths (Sect. 2.2). We then describe and discuss the spectra (Sect. 2.3), which display intense nebular lines and NIR/MIR rising continua. In Sect. 2.4, we discuss the uncertainties on the quantities measured from the images and from the spectra.

In Sect. 3, we perform a comparison of the data for the three YMCs in NGC 1365 with comparable data obtained for R136 in the LMC, one of the nearest known YMC. To do so, we use WFI and IRAC images, an ISO SWS spectrum and a wide field ISO CVF spectrum of R136. In Sect. 4, we derive basic parameters for the YMCs based upon their emission lines, via a comparison with predictions from a library of photo-ionisation models generated with the code `CLOUDY`. In Sect. 5, we analyse the NIR/MIR infrared emission of the sources, both their spectral energy distribution (SED) and their line emission, performing a more complex modelling with the dusty stellar population evolution code `GRASIL`. Then, in Sect. 6, we attempt to position our results in the light of the theoretical evolution of very massive clusters, considering the bi-modal hydrodynamic solution for re-inserted matter, as proposed by Silich et al. (2007) and Tenorio-Tagle et al. (2007). Finally, the conclusions and perspectives of our work are highlighted in Sect. 7.

2. The NIR/MIR dataset

Using the ESO infrared facilities, we obtained new images of the central region of NGC 1365, as well as spectra of the three MIR/radio sources reported by Galliano et al. (2005). With ISAAC, the NIR spectro-imager at VLT/UT1, we have collected J (1.2 μm)[1], Ks (2.2 μm), L' (3.8 μm) and M (4.5 μm)[2] images at an angular resolution of the order of 0.6″, and low resolution long slit spectra of the three MIR/radio sources, in the K and L bands[2]. Notice that throughout this paper, we retain the source nomenclature as in Galliano et al. (2005): the embedded sources are referred to as M4, M5 and M6. For one of the sources (M6), we also obtained a spectrum in the N band (around 10 μm)[3] with TIMMI2, the MIR spectro-imager of the 3.6 m telescope at La Silla: despite its rather low S/N ratio in the continuum, a prominent [NeII] line could be detected. This encouraged us to perform additional observations with VISIR at VLT/UT3, providing an image in the narrow [NeII] filter at 12.8 μm[4], together with low resolution spectra in the 8 μm, 11 μm and 12 μm bands[5].

In addition, we use in our analysis a WFPC2 R band image retrieved from the HST archive, the ATCA centimetre maps by Forbes & Norris (1998) and by Morganti et al. (1999), as well as the centimetre measurements of Sandqvist et al. (1995). We also consider the TIMMI2 10.4 μm, 11.9 μm and 12.9 μm images previously obtained by Galliano et al. (2005).

2.1. Data collection and reduction

All data were acquired and reduced using standard techniques. Let us briefly recall the main steps below:

ISAAC images: the images (J, Ks, L' and M bands) were obtained using the Aladin detector, with pixel scales of 0.148″ per pixel in the J and Ks bands and 0.071″ per pixel in the L' and M bands. The on-source integration times for the J, Ks, L' and M bands were respectively of 90 s, 300 s, 300 s, 450 s. A standard nodding technique was applied for the J and Ks observations, while chopping and nodding were used for the L' and M observations. All images were reduced with the `ECLIPSE` package. The photometric calibration of the images relied on observations of a standard star. The precision on photometric measurements is of the order of 10%. The achieved angular resolutions are 0.56″ in J, 0.44″ in Ks, 0.39″ in L' and 0.38″ in M. The M band image has a low S/N ratio though and is not used in the following.

ISAAC spectra: the low resolution long slit mode was used to collect Ks and L' band spectra of the sources M4, M5 and M6. Spectral resolutions were respectively R = 450 and 360 for the Ks and L' bands. Two positions of the 1″ width slit allowed us to obtain the three spectra: one slit at PA = 2.8° (PA positive from North to East) passed through the AGN and M4, while another slit at PA = 145.1° passed through M5 and M6. The slits were precisely positioned following the measurements in Galliano et al. (2005), and by performing blind offsets referenced on the AGN. Standard data reduction procedures were applied, using

---

[1] P074.B-0166; October 29, 30, 2004.

[2] P072.B-0397; December 01, 02, 2003.

[3] P074.B-0166; October 23, 24, 2004.

[4] P074.A-9016; December 01, 2004.

[5] P076.B-0374(A); November 18 and 20, 2005.

`ECLIPSE` and `IRAF`. In the *K*s band, self-chopping effects prevent us from assessing precisely the continuum level, although they do not affect the measurement of emission line fluxes. The spectra were extracted through slit windows of 1.4″ along the slits. Night-sky lines were used for the wavelength calibration.

TIMMI2 spectrum: with TIMMI2, an *N* band spectrum was obtained for M6, using the 10 μm low resolution grism (7.5 μm to 13.9 μm) with spectral resolution $R = 160$. The pixel scale is 0.45″. The slit, 1.2″ wide and at PA = 0°, was blindly positioned on the target using the AGN as a reference. The standard nodding and chopping technique allowed an efficient removal of the background emission. The on-source exposure time was about 4000 s. Subsequent data processing consists of the addition of chopping and nodding pairs, followed by a shift-and-add procedure to sum the two negative and one positive spectra generated by the chopping-nodding technique.

VISIR image: VISIR allowed us to collect an image of NGC 1365 through the narrow [NeII] 12.8 μm filter (*FWHM* of 0.2 μm). The standard chopping and nodding technique enabled us to remove the MIR background. The data reduction consists of shifting and stacking the individual frames (each corresponding to a chopping position). The achieved angular resolution is 0.4″. To optimise the detection of extended features, the image was filtered using the `mr_filter` routine of the `MR/1` software package developed by Murtagh & Starck (1999).

VISIR spectra: we chose for the VISIR spectra the same two slit positions as for the ISAAC spectra. We observed in three settings with wavelengths centred at 8.5 μm, 9.8 μm and 12.2 μm, in a low resolution mode ($\lambda/\Delta\lambda$ of the order of 200). Exposure times were respectively 655 s, 510 s and 516 s for the three settings. Doing so, we achieve the following spectral coverage: from 8.1 μm to 9.3 μm, and from 10.4 μm to 13.0 μm, with a good overlap around 11 μm. Observing procedures and data reduction techniques are similar to those described for the TIMMI2 spectra. The absolute calibration of the 12.2 μm centred spectrum was assessed through the calibrated VISIR 12.8 μm narrow band image. The 9.8 μm centred spectrum was then scaled, through its overlap with the 12.2 μm centred spectrum. For the spectrum centred at 8.5 μm, we retain the original flux calibration. Therefore, there is some uncertainty between the relative fluxes of the 8.1−9.3 μm and the 10.4−13 μm segments of the spectrum. The precision on the absolute calibration of the 10.4 to 13 μm segment is of the order of 20%, comparable to that of the VISIR image and better than that of the 8.1−9.3 μm segment. The calibration uncertainty for the latter spectral segment is mostly due to possible varying slit losses, and might reach 40%.

2.2. Analysis of the images and registration

Figure 1 displays a three colour image (0.6 μm, 2.2 μm and 3.8 μm) of the central region of NGC 1365. The northern dust lane appears in green (2.2 μm), while the three sources of interest show up in red. Figure 2 provides a summary overview of the imaging data. The large image presents the central 30″ × 30″ of NGC 1365 through the HST *F606W* filter (referred to as an *R* image since it is close to the standard *R* band filter). This image is the pipeline-reduced HST/WFPC2 archive image. The location of the bright type 2 AGN (Lindblad 1999) is at relative coordinates (0″; 0″). The square to the North of the AGN outlines the region where the three bright MIR/radio sources, M4, M5 and M6, are found. The series of small images offers closer views of this region at wavelengths: 0.6 μm (WFPC2), 2.2 μm (ISAAC), 3.8 μm (ISAAC) and 12.8 μm (VISIR), as well as a reprint of the 3 cm ATCA image from Forbes & Norris (1998). In these closer views, three pairs of concentric circles indicate the positions of M4, M5 and M6, and the aperture sizes used for the flux density measurements presented in Sect. 2.4.

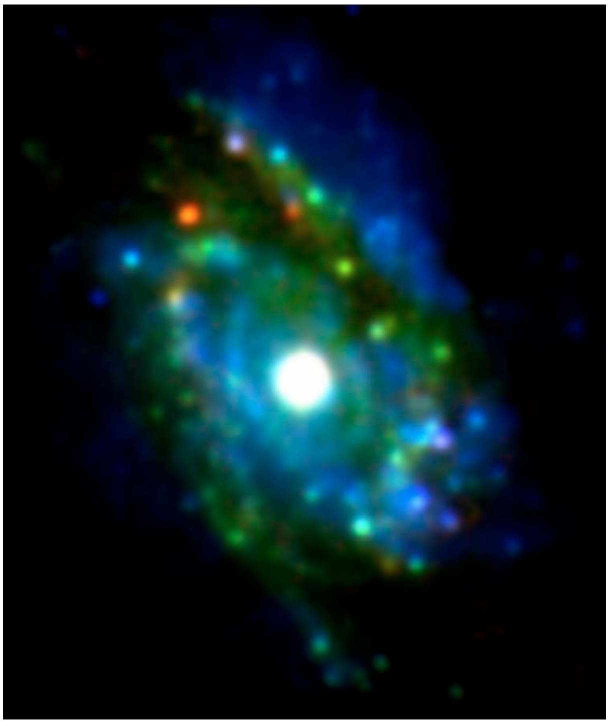

Fig. 1. Three colour image of the central region of NGC 1365. The WFPC2 *R* band image is blue, the ISAAC *K*s band image is green, and the ISAAC *L*′ band image is red. *North is up and East is to the left*. The dimensions of the image, 25″ × 30″ correspond to 2.25 kpc × 2.7 kpc for a distance of 18.6 Mpc.

The morphology of the nuclear region of NGC 1365 varies with wavelength. Hence, the relative registration of images at different wavelengths has to be performed with care. In the following, we do not provide absolute source positions but rather derive relative registrations. For image orientations and pixel sizes, we use the values attached to the image headers. On the *R*, *J* and *K*s band images, enough sources are detected in the field of view to allow good relative positioning. For this, we use the sources labelled C1, C2 and C3 in Fig. 2 which lie outside zones of highest extinction. We do not use the AGN itself to register these images, as a shift between its visible and infrared peak-positions may occur. On the other hand, in the *L*′ and *N* band images, only the AGN and the sources M4, M5 and M6 have a S/N ratio sufficient to perform positional measurements. In this case, the AGN must be used for registration and we make it coincide with its location on the *K*s band image (Fig. 3). In the modelling, this is an acceptable assumption as only a minor offset, if any, is to be expected for the AGN position between the *K*s and *N* bands (Granato et al. 1997).

Under such a registration, Fig. 3 shows that the positions of the reference sources C1, C2 and C3 agree within better than ±0.1″ in the *R*, *J* and *K*s band images. At longer wavelengths, as discussed above, one must rely on the location of the AGN and, assuming that offsets of the nuclear peak projected positions in the *K*s, *L*′ and 12.8 μm bands are small compared to the image resolutions, the global precision on the registration of all maps is better than ±0.1″. Estimates of the precision in the relative positioning do matter since, as shown in the three bottom rows of

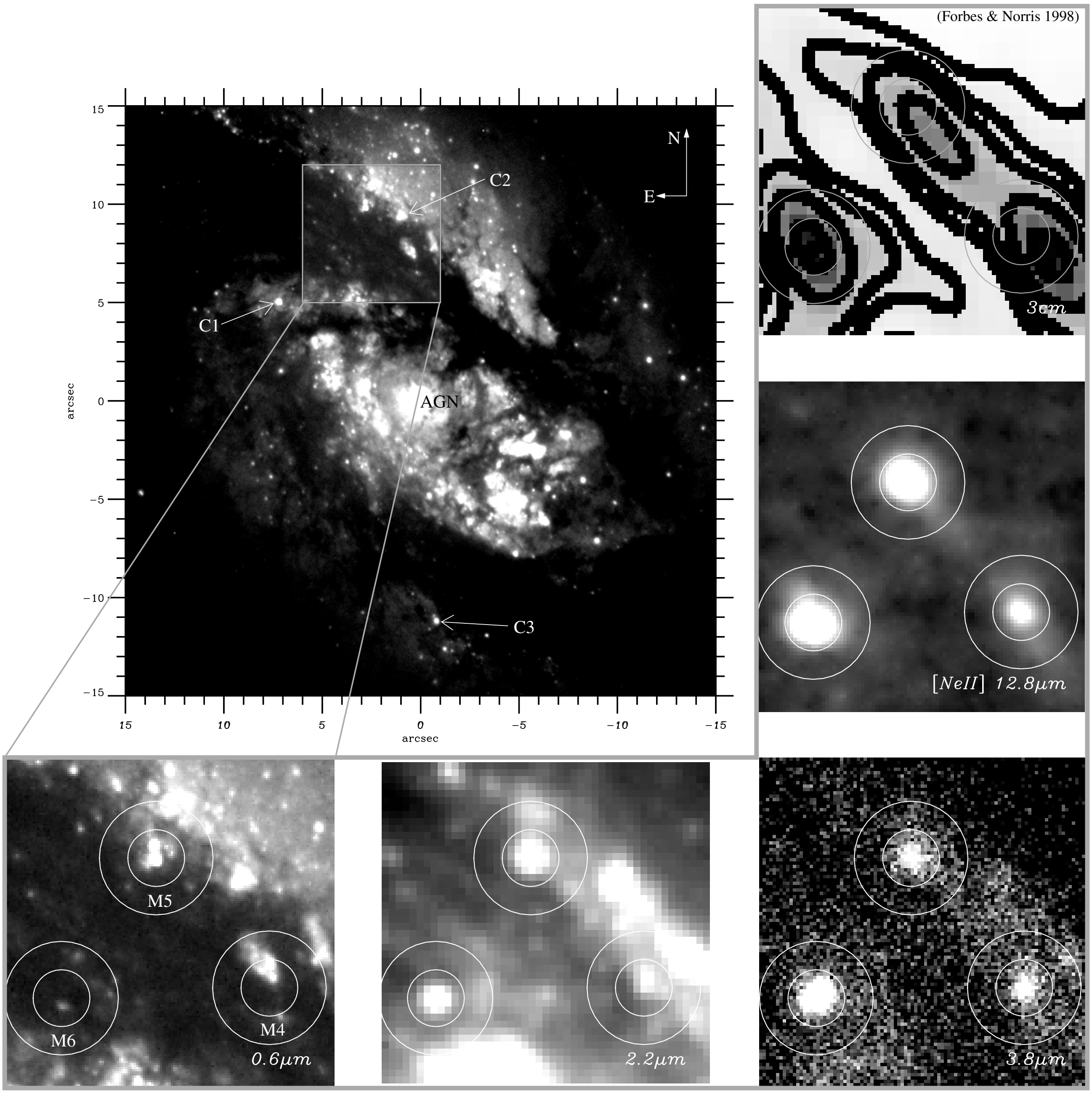

Fig. 2. The embedded clusters in NGC 1365. The large image shows the inner 30″ × 30″ observed with HST/WFPC2 in the *F606W* filter (0.6 μm). The highlighted square shows the region where the three embedded young massive star clusters M4, M5 and M6 are located. The small images detail this region at five wavelengths: 0.6 μm (HST/WFPC2), 2.2 μm (VLT/ISAAC), 3.8 μm (VLT/ISAAC), 12.8 μm (VLT/VISIR) and 3 cm (Forbes & Norris 1998, ATCA, reproduced from their work). For clarity, the *J* (1.2 μm) image mentioned in the text is not displayed here. Its angular resolution is rather low and adding it would not bring any pertinent information. The locations of M4, M5 and M6 are given by the centres of the concentric circles on the small images. They correspond to the locations of the 12.8 μm sources. Sources labelled C1, C2 and C3 as well as the active galactic nucleus (labelled AGN) are used for the registration (see Sect. 2.2).

Fig. 3, the positions of the peaks corresponding to M4, M5 and M6 appear to move slightly with wavelength. In the following, we call the "location" of M4, M5 or M6 the projected position of their corresponding 12.8 μm peak, provided in Table 1. They correspond to projected distances to the AGN of 640 pc, 920 pc and 760 pc for M4, M5 and M6 respectively.

In the *R* and *K*s bands, no obvious emission is detected at the exact location of M4. Notice that M4 is located close to, but not coincident with, the apex of a cone-shaped structure appearing on the *R* band image, roughly extended in the North-East direction. This structure is also bright in the *J* band. Emission in the *K*s band is detected between the location of M4 and the peak in the *J* band mentioned above. It may be a mixture of emission from M4 and from the "cone". The source M4 is clearly detected in the *L*′ band as well as at 12.8 μm.

The source M5 is detected in the *R*, *J*, *K*s and *L*′ bands and at 12.8 μm.

The source M6 is detected in the *K*s, *L*′ bands, as well as at 12.8 μm. Possible counterparts to M6 are detected, slightly offset to the South, in the *R* band (offset by 0.2″) and *J* band (offset by 0.1″).

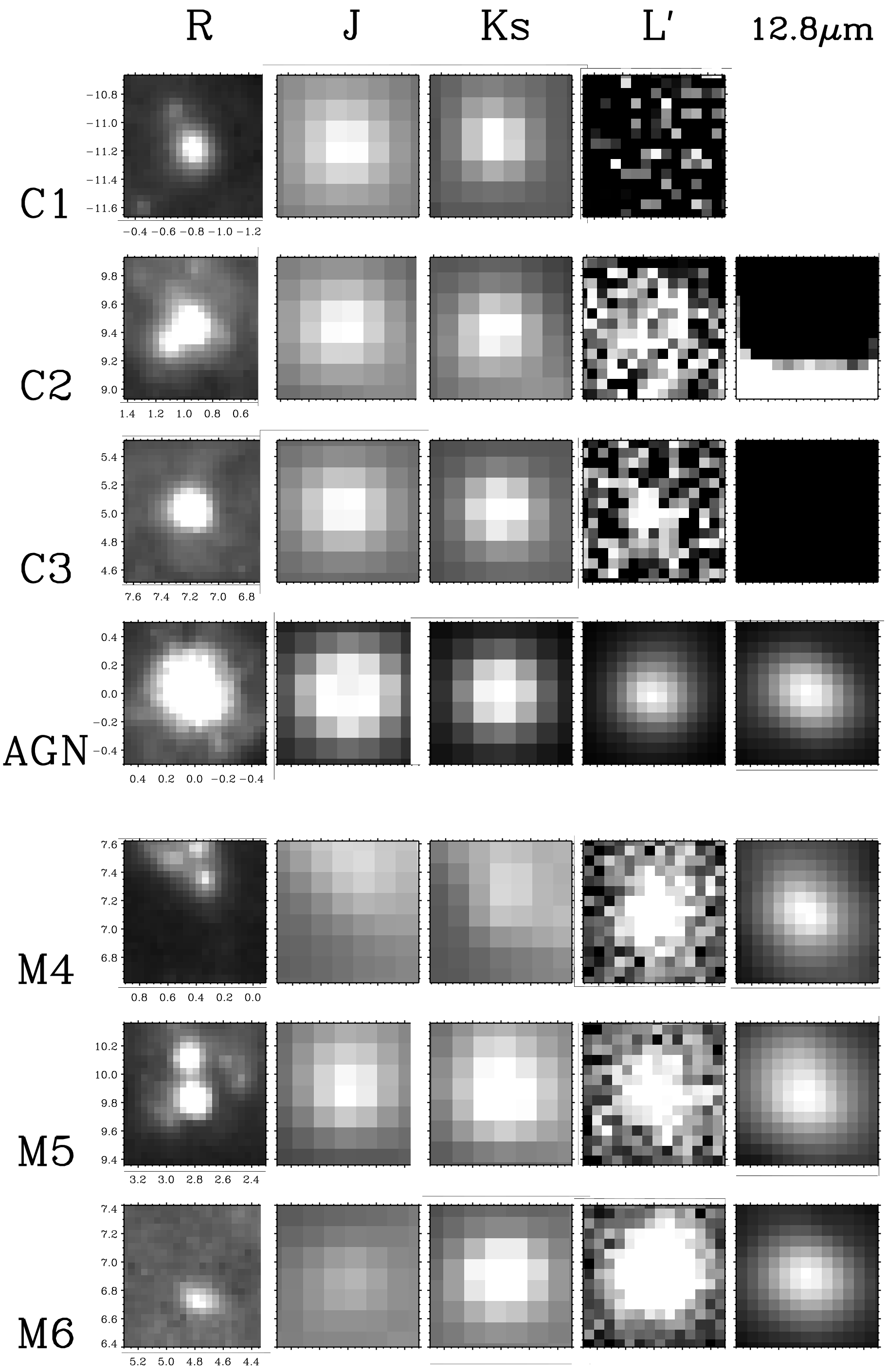

Fig. 3. Details of the different images illustrating, for C1, C2 and C3 the quality of the registration, and for M4, M5 and M6, the morphological changes that these sources suffer with wavelength. Each row shows the images of a given source at the various observed wavelengths. The wavelengths are *from left to right*: *R*, *J*, *K*s, *L*′ and 12.8 μm. The sources are *from top to bottom*: C1, C2, C3 (see Fig. 2), AGN, M4, M5, M6. The first four rows illustrate the quality of the registration. The last three rows highlight the morphological changes of the embedded YMCs with wavelength. The *X* and *Y* scales for each image represent the same coordinates as in Fig. 2, where (0″; 0″) coincides with the AGN location.

Regarding the 3 cm image, we only have access to the printed figures by Forbes & Norris (1998) and Morganti et al. (1999), therefore no precise measurement can be performed. Figure 4 presents the filtered 12.8 μm image with cuts highlighting the extended emission and compares this image to the 3.5 cm map by Morganti et al. (1999). The similarity of the two maps is striking, not only for the main peaked sources, but also for the extended emission and in particular for the western feature elongated in the North-East direction. The sources M4, M5 and M6 appear to be distributed in a well defined star-forming ring, delineated through its MIR/radio emission. The AGN itself is neither radio bright, nor clearly isolated on the radio image, and hence cannot be used for registration purposes. The two independent maps by Forbes & Norris (1998) and Morganti et al. (1999) are in good agreement. Both indicate that the three radio sources cannot be simultaneously made precisely coincident with the three MIR sources. In Fig. 2, M6 is chosen as the reference: M4 and M5 are slightly shifted to the North-East with respect to the radio map. In Fig. 4, we display an alternative solution in which M4 and M5 have precise radio counterparts: then, M6 appears to be slightly shifted to the South-West with respect to the radio emission. As each of the two independent radio maps shows this offset, in its comparison with the MIR image, we conclude that the offset is real, but remains to be understood.

The sources M4 and M6 appear to be located on the dust lane, in projection. The fact that, in the *R* band, M4 is not detected and M6 is very weak suggests that they lie inside the dust lane. The source M5 lies on the edge of the dust lane, and

Table 1. Measurements derived from the spectra.

	M4		M5		M6	
	value		value		value	
	low	high	low	high	low	high
position with respect to AGN [arcsec]						
$\Delta\alpha$ [arcsec]	0.31	0.51	2.70	2.90	4.70	4.90
$\Delta\delta$ [arcsec]	7.02	7.22	9.76	9.96	6.80	7.00
flux densities [mJy]						
R	≤0.10		0.13	0.19	≤0.05	
J	≤1.21		0.79	1.88	≤1.01	
Ks	≤1.18		0.62	1.47	0.31	1.29
L'	0.28	3.80	0.69	3.87	1.81	7.16
10.4 μm	0.57	3.94	41.33	62.90	37.18	57.01
11.9 μm	20.10	47.26	78.76	130.16	109.15	169.90
12.9 μm	91.97	169.03	208.83	341.28	379.61	575.43
12.8 μm	77.24	128.32	183.10	287.64	264.64	421.92
6 cm	2.38	2.98	1.12	1.72	2.45	3.05
20 cm	3.04	3.64	2.44	3.04	2.24	2.84
line fluxes [10^{-15} erg s^{-1} cm^{2}]						
Pα	23.18	34.76	64.64	96.96	60.43	90.65
Brδ	1.23	1.84	3.40	5.10	3.48	5.22
H_2 1-0S(3)	0.71	1.07	0.96	1.44	1.29	1.94
H_2 1-0S(2)	0.36	0.54	0.37	0.56	0.44	0.66
HeI	0.86	1.29	1.85	2.77	2.44	3.67
H_2 1-0S(1)	1.06	1.59	1.02	1.53	1.13	1.70
Brγ	2.71	4.06	5.87	8.81	6.84	10.26
H_2 1-0S(0)	0.38	0.57	0.43	0.64	0.52	0.78
H_2 2-1S(1)	0.27	0.40	0.31	0.47	0.31	0.46
H_2 1-0Q(1)	0.40	0.60	0.74	1.10	1.27	1.91
H_2 1-0Q(2)	0.33	0.50	0.44	0.66	0.52	0.78
H_2 1-0Q(3)	0.37	0.55	0.52	0.78	0.58	0.87
Pfδ	38.70	58.06	35.76	53.64	59.23	88.85
Brα	16.66	24.98	19.82	29.74	31.50	47.24
[ArIII]	≤12		≤11		≤12	
[SIV]	≤6		≤5		≤5	
[NeII]	110	170	440	660	570	850
[a]spectral indexes $F\nu \propto \nu^{-\alpha}$						
$\alpha_{2\ \mathrm{cm}}^{6\ \mathrm{cm}}$	–0.49	–0.29	–0.87	–0.67	–0.54	–0.34
$\alpha_{6\ \mathrm{cm}}^{20\ \mathrm{cm}}$	–0.29	–0.09	–0.66	–0.46	–0.03	0.17

[a] Spectral indexes from Sandqvist et al. (1995). An uncertainty of ±0.1 is added.

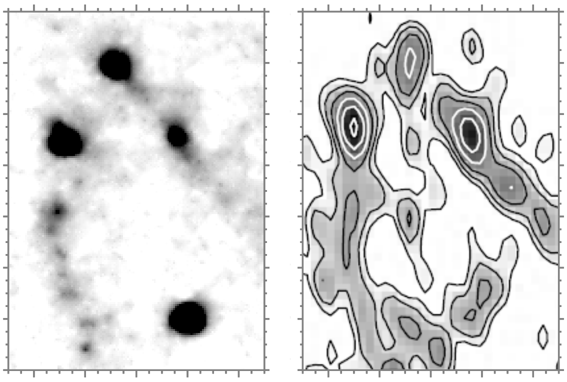

Fig. 4. Comparison between the VISIR narrow band 12.8 μm filter image (*left*) and the 3.5 cm map (*right*) by Morganti et al. (1999) for a 10″ × 14″ region including the AGN (*bottom source on the left image*), the three embedded YMCs and the MIR/cm ring. *North is up*, *East is to the left*. The ticks along the axis are drawn with 0.5″ intervals.

consistently appears less extinguished, showing a bright counterpart in the R band. Halos of emission are detected around M4, M5 and M6, both in the L' band and at 12.8 μm.

Thus, the relative positioning of the visible and IR images has been achieved at a precision of 0.1″ and is adopted in the following analysis.

We make some cautionary remarks in the case of M4: the comparisons between its maps indicate that aperture flux measurements should be unreliable in the R, J and Ks bands, where no clear counterparts are found and as it lies in the vicinity of an R band emitting cone and of a J to Ks band emitting region. We believe that, at these wavelengths (R, J and Ks bands), aperture flux measurements for M4 are upper limits.

The source M5 is well defined at all wavelengths. A neighbouring weak source to the North (seen on the R band image) may contribute some flux to its aperture flux measurements in the J and Ks bands. Yet, M5 probably remains the dominant source in the Ks band.

The source M6 is clearly detected at all wavelengths except in the R band. At this wavelength, a weak source is detected ~0.2″ to the South of the location of M6 (see Figs. 2 and 3). We cannot firmly exclude that it is an unrelated source, therefore its flux has been included in computing the R band flux upper limit of M6.

These remarks of course apply to continuum measurements from the spectra that we are about to discuss, since they correspond to a 1″ × 1.4″ aperture. This leads to the following

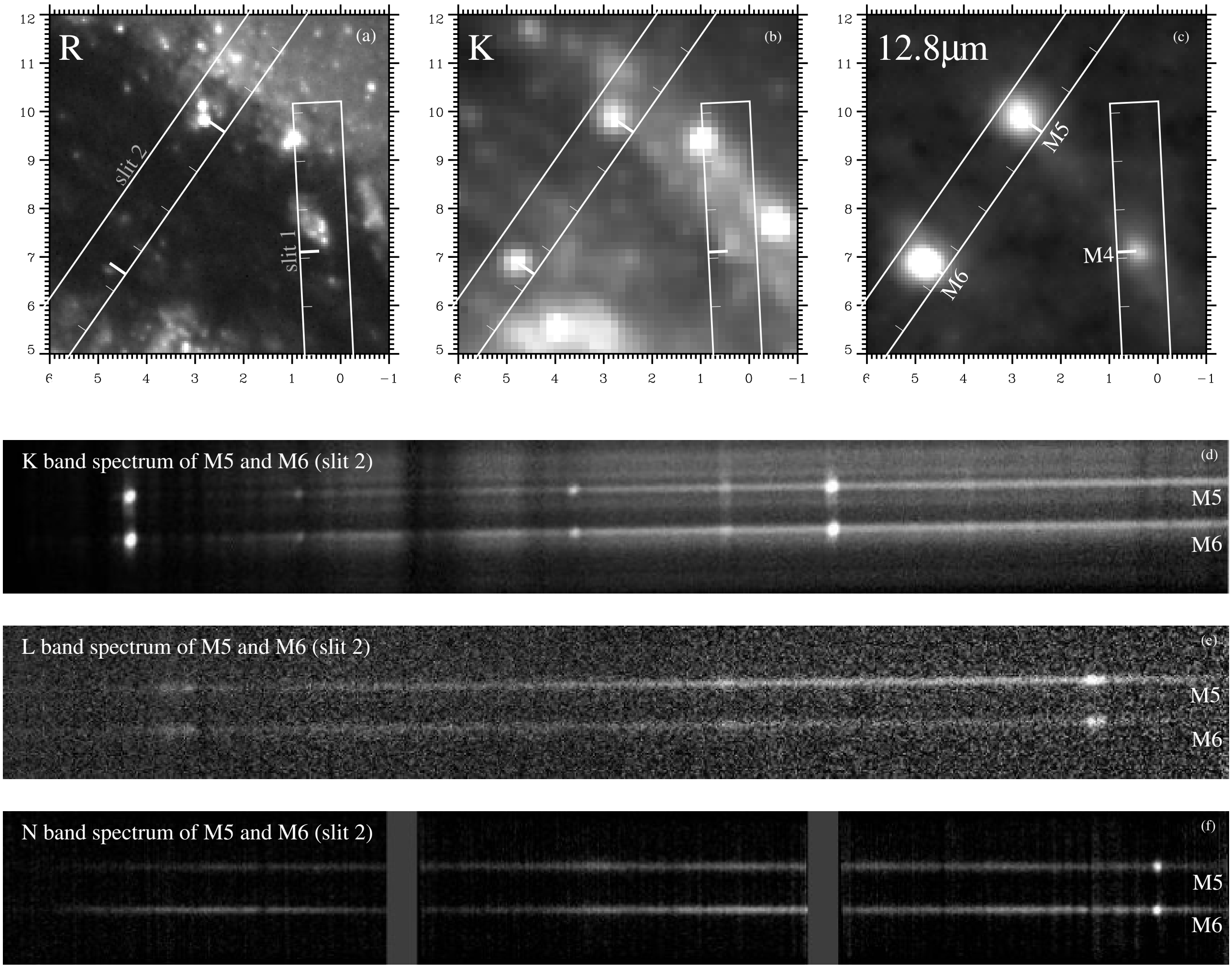

Fig. 5. *Frames* (**a**)–**c**)) *from left to right*: *R*, *K*s and 12.8 μm images of the embedded clusters region. *North is up and East is to the left*. The slit drawings show the positions of slit 1 (through the nucleus and M4) and slit 2 (through M5 and M6). Along the slits, the thin and short ticks mark a scale in arcsec, while the thick and long ticks mark the position where the spectra are recorded. The references are the nucleus for slit 1, and M5 for slit 2. *Frames* (**d**) and **e**)): ISAAC spectra through slit 2 after reduction and before extraction. The wavelength increases from *left to right*. In the *K*s spectrum, the two brightest lines are Pα and Brγ. This image shows that, due to self-chopping, it is difficult to assess the actual continuum level. In L', the bright line to the right is Brα. Since no extra emission is detected along the slit, apart from the two clusters, self chopping is inexistent. *Frame* **f)** VISIR spectra, from left to right separated by grey bands: 8.5 μm setting (8.1−9.3 μm), 9.8 μm setting (10.4−12.4 μm), 12.2 μm setting (11.3−13.0 μm). The bright emission line on the right is [NeII].

conclusion, to be kept in mind when interpreting the NIR spectra: in the case of M4, the *K*s band continuum is an upper limit, in the case of M5 it may be slightly overestimated, and in the case of M6 it is a proper estimate. At longer wavelengths, such issues are irrelevant.

2.3. Analysis of the spectra

In the upper part of Fig. 5, we provide drawings of the slits used for the spectroscopy in the *K*s and L' bands, superimposed on images in the *R* and *K*s bands and on the 12.8 μm image. Along the slits, thin ticks are drawn every arcsec, while longer and thicker ticks highlight the positions at which emission line spectra have been recorded. References used for the positioning of the spectra along the slits are the AGN for slit 1 and M6 for slit 2. M6 is a good reference since its position is well defined and does not shift significantly with wavelength above 1 μm.

For M4, the emission line spectrum position (given by the thick tick mark on the slit drawing) coincides with the emission peak on the 12.8 μm image; it is located 0.1−0.2″ to the South of an emission knot in the *K*s band (but itself has no clear counterpart in *K*s); it is also located 0.2″ to the East of the apex of the cone-shaped structure seen in the *R* band image.

The emission line spectrum at the position of M5 corresponds to well defined emission knots in the three images (*R*, *K*s and 12.8 μm).

The emission line spectrum at the position of M6 corresponds to an emission knot both in the 12.8 μm and *K*s images, but is 0.1−0.2″ to the North of an emission knot in the *R* image.

The 2D raw spectra obtained through slit 2 in the *K*s and L' bands with ISAAC, and in the *N* band with VISIR, are displayed at the bottom of Fig. 5. The brightest emission lines identified in the figure are Pα and Brγ in the *K*s band, Brα in the L' band and [NeII] in the *N* band.

The extracted spectra are displayed in Figs. 6–8 for M4, M5 and M6 respectively. The following set of emission lines is detected: (a) nebular lines Pα, Brδ, HeI, Brγ, Pfδ, Pfγ, Brα, [NeII] 12.8 μm; (b) molecular lines from H_2 and (c) PAH emission. We detect PAH signatures at 3.3 μm and 11.3 μm. The

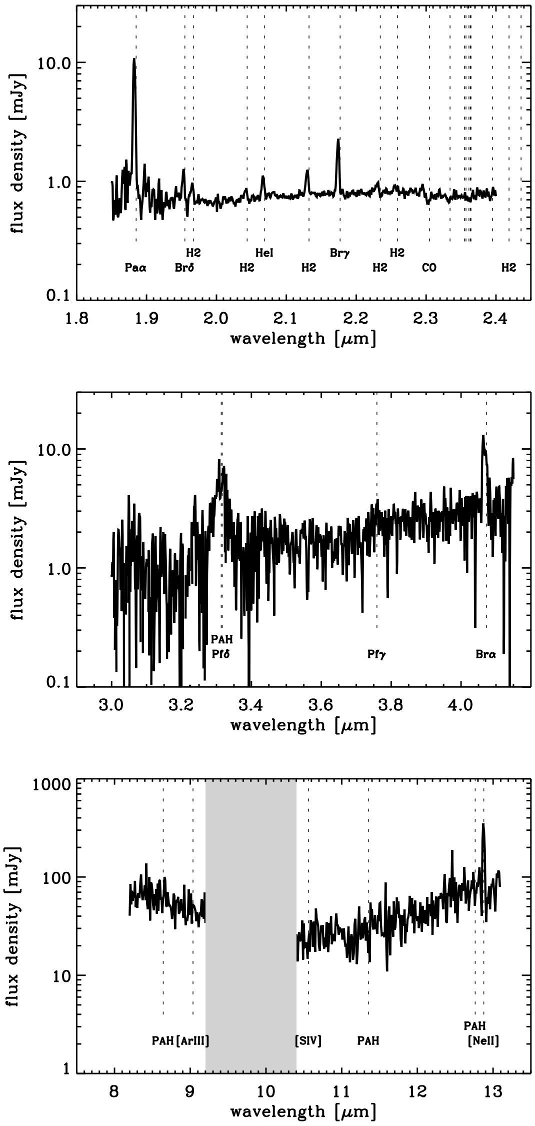

Fig. 6. *From top to bottom*, *K*s, *L′* and *N* band spectra of M4.

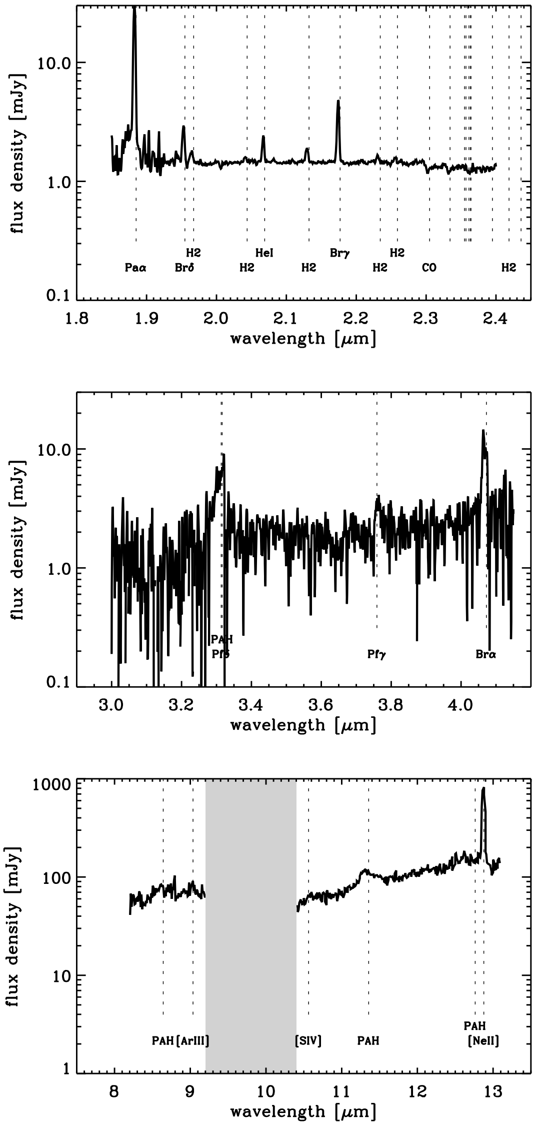

Fig. 7. *From top to bottom*, *K*s, *L′* and *N* band spectra of M5.

bump-like feature on the 8−9 μm spectrum of M6 might be a signature of the 8.6 μm PAH, although it looks too broad. Even though the [NeII] 12.8 μm line is bright, we do not detect any [ArIII] 8.9 μm or [SIV] 10.5 μm line emission, which is a puzzling and interesting result. The 12.7 μm PAH feature, expected to show up as a broad feature, is also absent. For the three sources, the continuum spectral distribution is flat or slightly rises with wavelength in the *K*s band and clearly rising in the *L′* and *N* bands. The presence of the 9.7 μm silicate absorption band is inferred in M4, M5 and M6, from the simultaneous fall and rise of the 8.1−9.3 μm and 10.4−13.0 μm continua respectively matching the blue and red wings of the silicate absorption feature. For the continuum in the *K*s band, one must bear in mind the remarks given at the end of the previous section. Between 3 μm and 3.3 μm, the transmission of the atmosphere is poor: this part of the spectrum is noisier and we think that the uncertainty on the atmospheric correction induces a supplementary error on the continuum value. We are tempted to believe that only the segment of the spectrum red-wards of 3.3 μm is reliable. In the *N* band, the spectral calibration for the red side of the spectrum has been performed through scaling to the VISIR narrow band 12.8 μm image and taking advantage of the overlapping region between 11 μm and 12 μm. This procedure resulted in applying scaling factors to the spectra. Such a correction cannot be applied to the blue side of the *N* band spectrum, since no overlapping spectrum is available. Therefore, the relative scaling between the 8.1−9.3 μm segment and the 10.4−13 μm segment of the spectrum may be uncertain by a factor of up to 2.

In the spectra, an interesting feature is the extension of the line emission along the slit direction (see the *K*s band spectrum in Fig. 5) for the brightest lines. For M4, and in spite of a rather low spectral resolution, we can even detect a velocity gradient in the Pα line. The position-velocity diagram for the M4 Pα emission line is displayed in Fig. 9. Between positions $-1''$ and $+1''$, a velocity difference of the order of 100−200 km s^{-1} is measured. This kinematical feature will be discussed elsewhere. In the case of M5 and M6, we also detect extended nebular emission (see Fig. 5), but no velocity gradient.

Spectral analysis in the radio domain would also be of great interest. The radio measurements by Sandqvist et al. (1995) indicate that the spectral indexes in the three sources flatten with increasing wavelength, suggesting optically thick radio emission. Unfortunately, such measurements are difficult from an

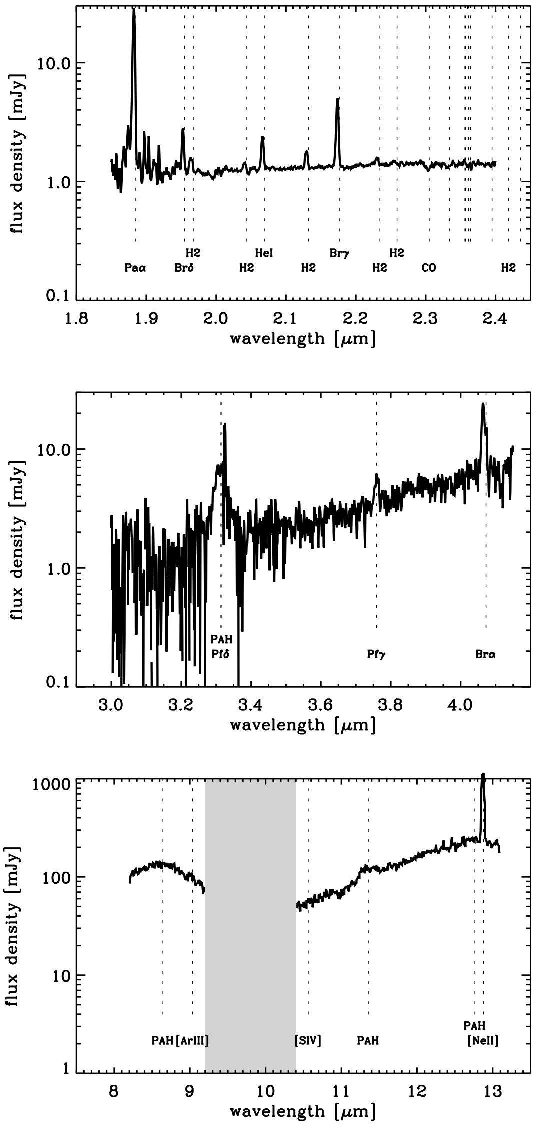

Fig. 8. *From top to bottom*, *K*s, *L*′ and *N* band spectra of M6.

image with a complex brightness distribution and have not been repeated by Morganti et al. (1999), hence cannot be double checked.

In summary, the collected spectra exhibit bright nebular and molecular emission lines at the location of the MIR/radio sources M4, M5 and M6: this reinforces the idea that these sources are embedded YMCs. The line emission is spatially extended; in the case of M4, a velocity gradient over a few arcsec is detected, suggesting the presence of an outflow.

2.4. Measurements and related uncertainties

Table 1 displays the full set of measurements performed for the three sources M4, M5 and M6. The flux density measurements were made through apertures of 0.6″ radius, represented in Fig. 2 by the small inner circles, and centred on the source positions as determined on the VISIR 12.8 μm image. Fluxes were measured on the following images: the HST/WFPC2 *R* band image, the ISAAC *J*, *K*s, *L*′ band images, the TIMMI2 10.4 μm, 11.9 μm and 12.9 μm images (Galliano et al. 2005), and the VISIR 12.8 μm image. In Galliano et al. (2005), we suspected the 12.9 μm flux densities to be overestimated by a factor 2. The TIMMI2 *N* band spectrum allows a direct measurement of the 11.9 μm/12.9 μm flux ratio (independent of the flux calibration), and shows that our suspicion was indeed founded. Therefore, the 12.9 μm fluxes for NGC 1365 quoted in Galliano et al. (2005) must be decreased by a factor of 2.

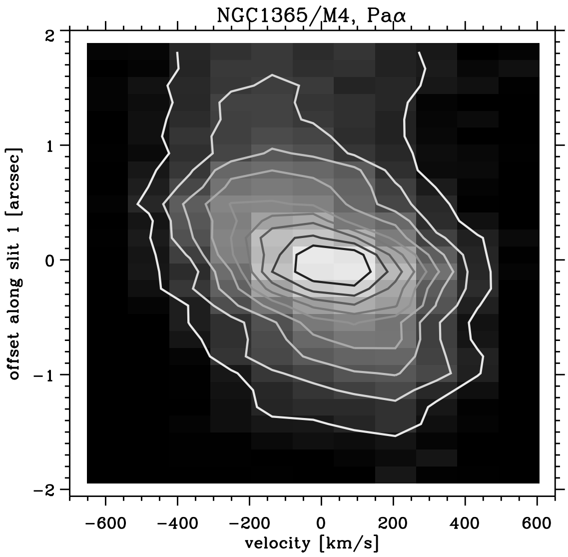

Fig. 9. Position-Velocity (Pα line) diagram for M4 along slit 1 (PA = −2.8°). The *X*-axis represents the velocity, the *X*-0 value being set at the emission peak. The *Y*-axis represents the spatial direction, top corresponding to the North. The *Y*-0 coordinate corresponds to the emission peak, also marked by a thick tick along the drawing of slit 1 in Fig. 5. At any position, the instrumental broadening is dominant (660 km s^{-1}).

Around each aperture, a “background” level was estimated by computing the median pixel value in an annulus with radii 0.6″ and 1.2″ around the aperture centre. The large and outer circles in Fig. 2 represent the outer borders of such annuli. We cannot be certain that this “background” also affects the source within the small aperture, as its origin and its location with respect to the source are unknown. Therefore, in a conservative approach we provide two flux density measurements for the sources M4, M5 and M6: one after “background” subtraction and one without “background” subtraction. The two figures for each flux represent the measurement uncertainty resulting from an ambiguity in the interpretation. To this uncertainty we add quadratically the uncertainty due to the photometric calibration. The calibration uncertainties used for the different bands are as follows, *R*: 10%, *J*: 10%, *K*s: 20%, *L*′: 20%, 10.4 μm: 20%, 11.9 μm: 20%, 12.9 μm: 20% and 12.8 μm: 20%. Whenever at a given wavelength no counterpart is clearly identified at the position of the MIR source, then we consider the high value of the error bar as an upper limit. In Table 1, the low and high values given for each measurement correspond to the lower and upper limits for the given measurement due to the uncertainties defined above.

Table 1 also provides the flux measurements for the emission lines identified in the spectra of M4, M5 and M6. In the case of M6, we have additional measurements for lines in the *N* band. Finally, we recall in this table the radio measurements published by Sandqvist et al. (1995). Figure 10 displays, for the three embedded YMCs, their SED together with their combined spectrum, covering in total a range from 0.5 μm to 13 μm. We briefly discuss the comparison between SEDs and spectra. The SED points show flux density values that we believe correspond

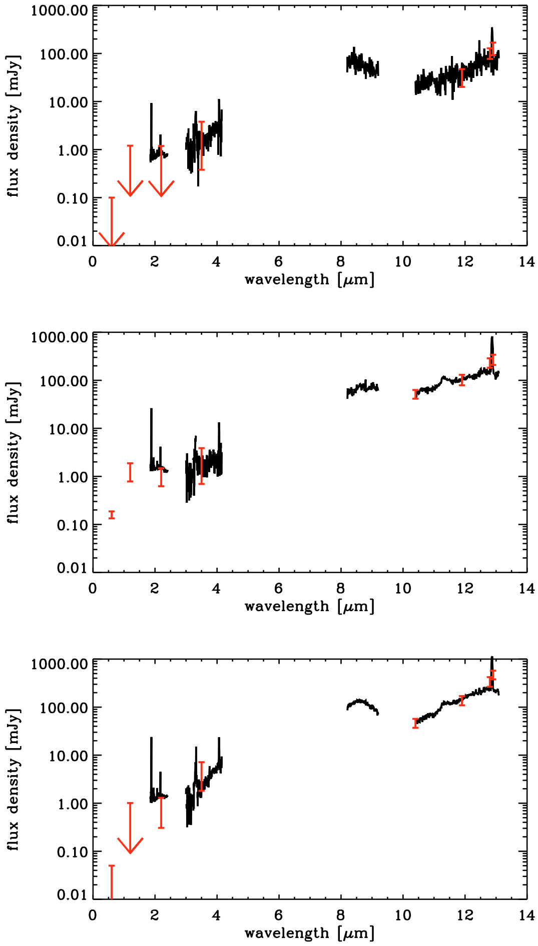

Fig. 10. NIR/MIR SEDs of the embedded clusters M4, M5 and M6 in NGC 1365 (red points with error bars or upper limits), over-plotted on the *K*s, *L′* and *N* band spectra (black continuous line). The NIR measurements are from this article, while the MIR points are from Galliano et al. (2005). For M4, since no direct *K*s band counterpart is observed on the image, the photometric point is given as an upper limit. This apparent inconsistency denotes the fact that we do not formally associate the *K*s band continuum with the cluster emission (see text).

directly to the sources of interest. However, in some cases they may correspond to upper limits because of source confusion. On the contrary, the spectra contain effective signal from the source and its surrounding. This distinction is particularly relevant in the case of M4. That is why in Fig. 10, for M4 the *K*s band spectrum is shown as an upper limit. For the sources M5 and M6, the *K*s band continuum corresponds to the upper part of the error bar on the flux measurement, because this value corresponds to the measurement performed without "background" subtraction. The *L′* band data points and the *N* band data points of Galliano et al. (2005) are in excellent agreement with the spectra. The TIMMI2 10.4 μm flux density for M4 is not reported in this figure, since there was no detection on the TIMMI2 image and the then quoted upper limit of 5 mJy may have been underestimated.

3. Comparison with a resolved young massive cluster: R136 in the LMC

The fact that the MIR/radio sources M4, M5 and M6 in NGC 1365 exhibit nebular lines strongly supports an interpretation in terms of embedded YMCs still hosting a fair fraction of ionising stars, hence younger than 10 Myr.

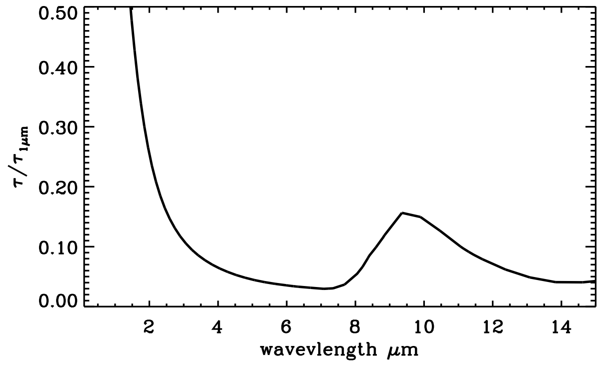

Fig. 11. Extinction curve used in this paper. This curve has been derived with `GRASIL` for the average Galactic extinction (Draine & Lee 1984).

We start the analysis by comparing the available data for the YMCs in NGC 1365 with similar information (images and spectra) of R136, a young cluster in the LMC. Basic parameters for these clusters will be derived in subsequent sections.

R136 is one of the nearest examples of a young massive cluster. It lies in the most luminous star forming region in the Local Group: 30 Doradus in the LMC, at a distance of 50 kpc. R136 has an age in the range 1−3 Myr and a stellar mass of $5 \times 10^4\ M_\odot$ (Boulanger & Rubio 2006).

Even though R136 is not properly speaking an embedded cluster, it is an interesting object for comparison with the MIR/radio emitting sources of NGC 1365. A three colour map of R136 is displayed in Fig. 12, built as a composite of two archived images obtained with the Wide Field Imager (WFI) at the 2.2 m telescope on La Silla (ESO) and one archived image collected with IRAC on board the Spitzer space telescope (NASA). Green codes the WFI *V*-band image (tracer of the stellar component), blue codes the WFI Hα image (tracer of the ionised gas) and red codes the IRAC 8.0 μm image (tracer of dust). The resolution of the WFI images has been degraded to 3.2″, which is the resolution of the IRAC 8.0 μm image. The composite field size is 10′ × 10′, which corresponds at the distance of the LMC to 145×145 pc^2. This field projects into a region of 1.6″ × 1.6″ at the distance of NGC 1365. This image shows that, even if R136 does not qualify as "embedded" cluster, it is a bright source of MIR radiation: would it lie behind or within an extinction lane, it would indeed be identified as an "embedded" cluster. This suggests that the MIR emitting dust of a so-called "embedded" cluster may not be necessarily in direct relation to the "embeddedness" of the cluster, as assumed in the typical cocoon-like view of an embedded cluster. As highlighted on this colour image, the three components are spatially separated: one can clearly identify the Hα emitting gas, spatially correlated with but distinct from the MIR dust component, and the stellar cluster itself. The wide dust shell (bubble) pushed by the cluster is prominent, while the Hα emission shows up as a thin layer at its inner rim.

Of the many spectra available for R136, let us consider: (i) the ISO SWS spectrum of a 14″×20″ region in the North-East MIR emitting lobe (shown by an arrow in Fig. 12) and (ii) the ISO CVF spectrum of the 3′ × 3′ region around the central cluster, covering the wavelength range from 2 to 16 μm (taken from Fig. 3 of Boulanger & Rubio 2006).

Notice that an aperture of 3′ × 3′ in the LMC translates to 0.5″ × 0.5″ at the distance of NGC 1365. This allows a direct comparison between the CVF spectrum of R136 and the ISAAC/VISIR spectra of the embedded YMCs in NGC 1365. Figure 13 displays the SWS and CVF spectra of R136

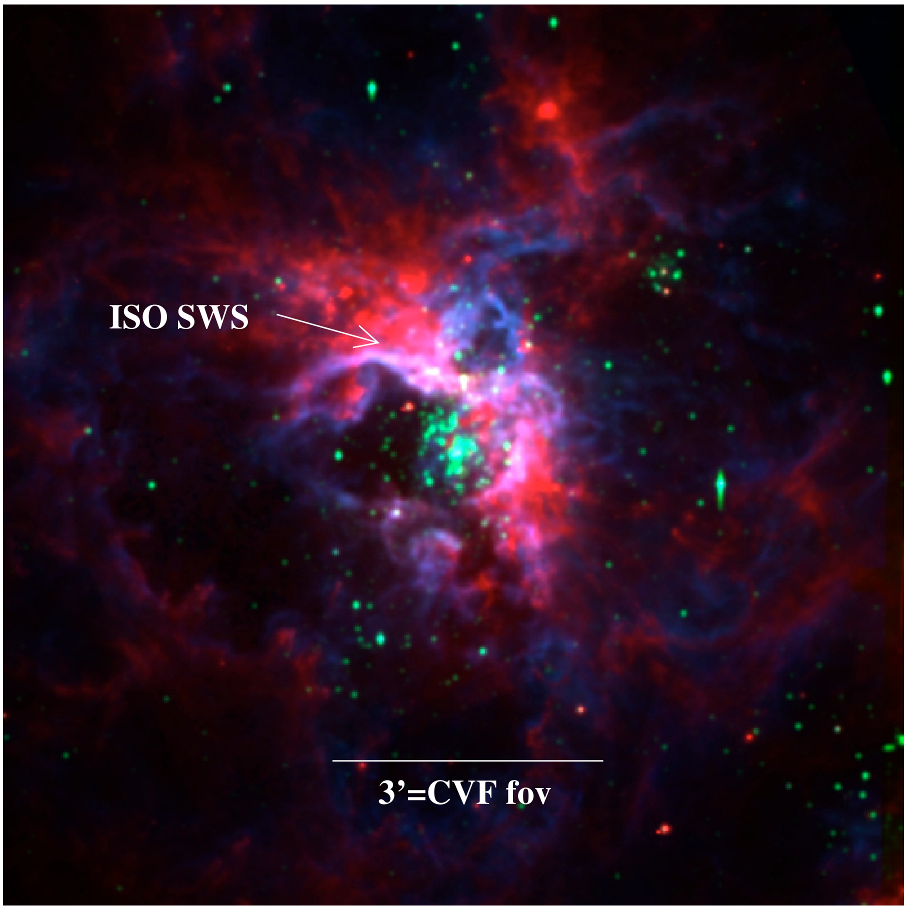

Fig. 12. ESO 2.2 m WFI/Spitzer IRAC view of R136 in the Large Magellanic Cloud. The field of view is 10′ × 10′. *North is up and East is to the left*. This region (145 pc × 145 pc) would project onto a field of 1.6″ × 1.6″ at the distance of NGC 1365. Blue codes the WFI Hα image, green the WFI V image and red the IRAC 8.0 μm Spitzer image. The 3′ scale corresponds to the aperture size of the CVF spectrum aperture and the arrow shows the location of the 14″ × 20″ ISO SWS spectrum aperture.

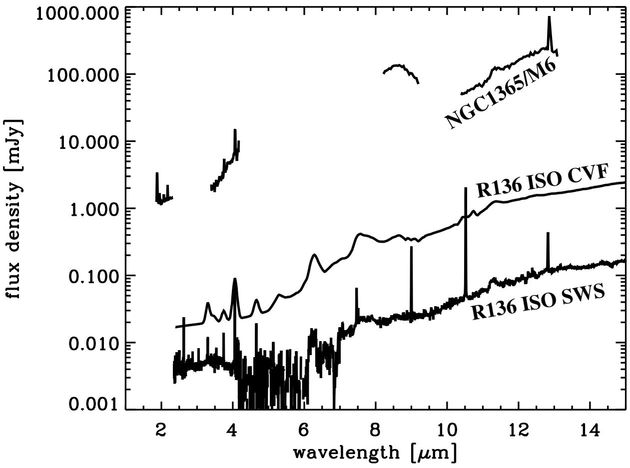

Fig. 13. Comparison of the ISAAC/VISIR spectrum of NGC 1365/M6, the ISO CVF spectrum of R136 and ISO SWS spectrum of R136. The spectra of R136 are projected to the distance of NGC 1365.

projected at the distance of NGC 1365, as well as the spectrum of N1365/M6. This comparison shows that M6 is, intrinsically, almost two orders of magnitude brighter than R136 and that, given the available data, the two sources exhibit at first order a rather similar spectrum. A remarkable difference, though, is the fact that in the 8−13 μm wavelength range, three bright emission lines are detected in the SWS spectrum of R136 ([ArIII] at 8.9 μm, [SIV] at 10.5 μm and [NeII] at 12.8 μm) while only the [NeII] 12.8 μm line is observed in the case of M6. This difference holds true in the case of M4 and M5. Owing to its low spectral resolution the R136 CVF spectrum does not show any of the narrow forbidden lines but only broad features such as the PAH bands.

We provide in Fig. 14 a comparison of the WFPC2 R and the [NeII]12.8 μm images of M5 with the WFI Hα and the IRAC 8.0 μm images of R136 projected at the distance of NGC 1365, with the same seeing and same pixel size as the M5 images. For this comparison we have chosen M5 since, among the three YMCs in NGC 1365, it is the one with the brightest visible counterpart, hence the closest to the evolutionary stage of R136. On the left side of Fig. 14, the images of M5 are displayed, while on the right side, the corresponding degraded images of R136 are shown. Notice that the bulk of the 8.0 μm emission in R136 looks elongated, while its counterpart in M5 is unresolved. The same occurs with the visible image: at the resolution of HST, the degraded R136 looks slightly more extended than M5. This comparison suggests that, in terms of intrinsic properties, the YMCs in NGC 1365 are slightly smaller than R136 while they are about two orders of magnitude brighter: they definitely deserve to be called “compact”. Another piece of evidence comes from the HST image, where M5 remains unresolved, at a resolution of 0.11″, which corresponds to about 10 pc. The fact that the sizes of the YMCs in NGC 1365 are comparable to, or even less than, that of R136, which is 100 times fainter, supports the idea that star cluster sizes do not depend on mass (Larsen 2004).

This simple and direct data comparison between the MIR/radio sources in NGC 1365 and R136 adds support to the interpretation of the NGC 1365 sources in terms of compact YMCs.

An additional striking difference between the two sources is the absence of the [ArIII] and [SIV] line emission in the YMCs

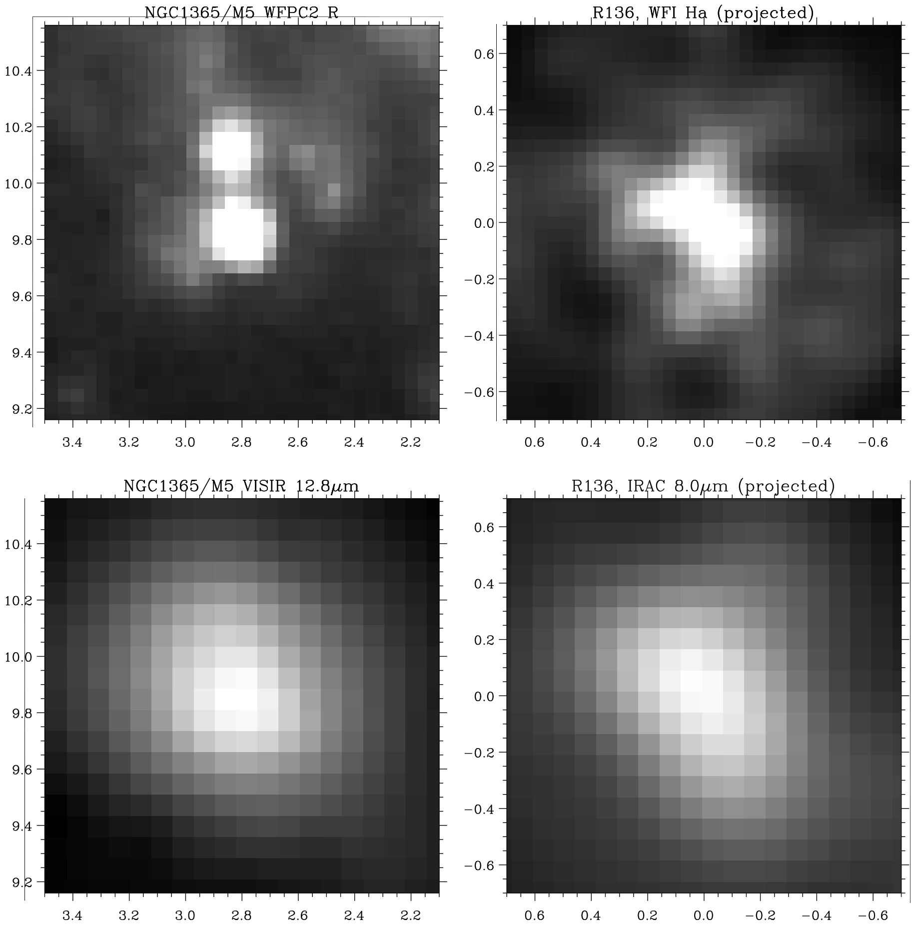
NGC1365/M5 WFPC2 R
R136, WFI Ha (projected)
NGC1365/M5 VISIR 12.8μm
R136, IRAC 8.0μm (projected)

Fig. 14. Map comparison between NGC 1365/M5 (*left column*) and R136 projected at the distance of NGC 1365. The R136 WFI Hα image and IRAC 8 μm image, after projection at the distance of NGC 1365, have been degraded to the seeing and pixel size of the NGC 1365/M5 WFPC2 R image and the VISIR 12.8 μm image respectively.

in NGC 1365. This important difference is discussed in Sect. 4 and explained through an age effect, the clusters in NGC 1365 being older than R136. A detailed comparison of the SEDs of R136 and of the YMCs in NGC 1365 is performed and included in Sect. 5.

4. Derivation of the YMC basic parameters

In this section, we attempt to derive parameters for the YMCs in NGC 1365, such as extinction, age and mass, using their emission line flux measurements. We make the gross assumption that a uniform foreground emission is affecting in a similar way all the emitting components in the cluster. This is obviously an oversimplification, but it leads to first-order interesting conclusions while avoiding to use model-fitting with too many free parameters. We shall turn to a more realistic modelling in the next section.

4.1. Extinction

First, we use the Brγ and Brα line measurements to derive the extinction towards the YMCs. We know already that they are located in a region of high extinction, in the vicinity of, or within the prominent East-West dust lane to the North of the AGN (Fig. 2). In the following discussion, we use the extinction curve derived with `GRASIL` (Silva et al. 1998) for Galactic dust. This curve is shown in the NIR/MIR range in Fig. 11.

A direct estimate of the extinction towards the embedded cluster nebular gas can be retrieved from the Brγ/Brα line ratio, assuming optically thin conditions for the nebular gas itself. This ratio depends only mildly on the gas density. Moreover, considering that the temperature of HII regions tends to cluster around $T_e = 10^4$ K (Osterbrock 1989), the predicted line ratio of Pα (1.87 μm) to Brδ (1.94 μm) is 0.0545. The differential reddening between Pα and Brδ is small, the two lines being quite close in wavelength, so we can use the directly measured Pα/Brδ ratio to check the conditions in the gas, and the validity of assuming the case-B line ratios. For the embedded clusters M4, M5 and M6, the measured ratios are respectively 0.053, 0.053 and 0.058, in good agreement with the theoretical value 0.0545 mentioned above.

Consequently, the case-B assumption looks adequate and we can confidently derive the extinction towards the embedded cluster nebular gas using the theoretical Brγ/Brα flux ratio of 0.35 (Osterbrock 1989). For M4, M5 and M6, we obtain NIR extinctions of $A_V = 13.5, 3.2$ and 8.5, respectively.We use these values to de-redden the NIR line fluxes.

4.2. Age and mass

Together with Brγ and Brα, we can use the measurements of the MIR fine structure lines [ArIII] 8.9 μm, [SIV] 10.4 μm and [NeII] 12.8 μm in order to derive the cluster parameters. Predicting the intensities of the fine structure lines is more complex than in the case of the hydrogen lines. Their ionisation potentials are larger (respectively 27.6 eV, 34.8 eV and 21.6 eV), which implies that not only the H ionising luminosity, QH, must be taken into account, but also that the shape of the ionising continuum must be known or assumed. Moreover, the fluxes in these lines depend on the ionisation factor, closely linked to the

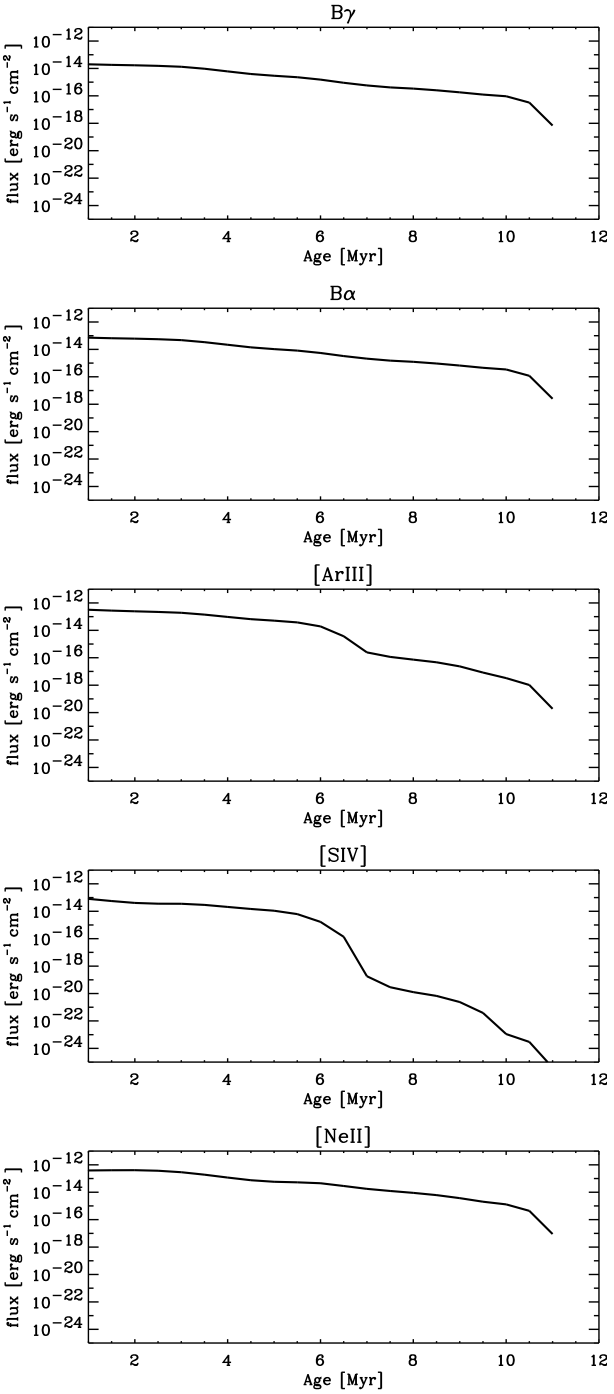

Fig. 15. Predicted line fluxes for the model described in Sect. 4.2. *From top to bottom*: Brγ, Brα, [ArIII], [SIV] and [NeII]. The X-axis displays the age in Myr and the Y-axis provides the line flux, at the distance of NGC 1365, corresponding to a 10^6 $M_\odot$ cluster.

geometry of the source, while we do not have much information on this value. Finally, the line fluxes depend on the element abundance ratios: given the location of the YMCs in their host galaxy, a set of solar abundances appears adequate even though a slight overabundance (up to a factor of two) could be expected.

What is remarkable on the spectra of the three sources, M4, M5 and M6, is that while the [NeII] line is conspicuous, only upper limits can be measured for the [ArIII] and [SIV] lines: the [NeII]/[SIV] line ratios are greater than 20, 100 and 140 for M4, M5 and M6 respectively, and the [NeII]/[ArIII] line ratios are larger than 10, 50 and 60. Such ratios are impossible to reproduce with very young stellar populations, for which the line ratio [NeII]/[SIV] is usually found to be lower than unity (see the SWS spectrum of R136 and for instance the spectrum of NGC 5253 in Martín-Hernández et al. 2005). So, a substantial difference in the line ratios is observed, by one to two orders of magnitudes.

In order to examine this difference, we use the `CLOUDY` emission line libraries computed by Panuzzo et al. (2003)[6] for use with `GRASIL` (Silva et al. 1998). In these libraries, the ionisation factor is varied by changing the gas density and the gas filling factor. Panuzzo et al. (2003) demonstrate that different geometries with a similar final ionisation factor will produce very similar line fluxes. We compute the Brγ, Brα, [ArIII], [SIV] and [NeII] line fluxes for a "cluster model" at ages between 1 and 10 Myr with an "instantaneous" star formation history. As mentioned above, we adopt solar abundances and we notice that in no way could an overabundance by a factor two account for the very large observed differences in line ratios.

Since the [ArIII]/[NeII] line ratios observed in M4, M5 and M6 are very small, we use the libraries predicting the smallest values for this ratio: a filling factor of 10^{-3} and density of 10^4 cm^{-3}. The evolution with age of the unextinguished line fluxes, at the distance of NGC 1365, is displayed in Fig. 15, for a total mass of stars of 10^6 $M_\odot$. To first order, these line fluxes show, for reasonable values, little dependence on the amount of gas, in agreement with the ionisation-bound situation.

In Fig. 16, we present a comparison between the modelled line fluxes and the observed ones. The procedure for building this figure for the three YMCs in NGC 1365 was the following:

- the extinguished modelled line fluxes are computed, for each YMC, with the related extinction value derived above;
- the extinguished modelled line fluxes are then normalised by changing the cluster mass, so that the modelled Brγ line flux equals the observed Brγ flux;
- the line ratios between observed and modelled line fluxes are then computed for each age and plotted (left Y-axis) as a function of age. Whenever the modelled flux falls inside the observational error-bar or is lower than the detection upper limit, then the ratio is set to unity;
- for each age, the corresponding stellar mass is also plotted (right Y-axis).

The model can be considered to "fit" the data if all three ratios are equal to one. This is not possible before 6 Myr, where we would expect intense [ArIII] and [SIV] lines, one order of magnitude brighter than allowed by the upper limits measured in the spectra of the three YMCs. A reasonable "fit" can be obtained only for ages greater than 6 Myr. Notice that in the case of M5, there remains a small discrepancy, by a factor of two, for the [NeII] flux, which, given the large differences involved and the first-order matches performed, is left aside.

In Fig. 17, we plot the Starburst99 spectra of an instantaneously formed Salpeter star cluster at ages 4, 5, 6 and 7 Myr, and compare them with the ionisation energy of [NeII], [ArIII] and [SIV]. This figure shows, between 5 and 6 Myr, a huge drop of luminosity (of about two orders of magnitude) for the continuum in the region of the ionisation energies for [ArIII] and [SIV]. On the contrary, the continuum around the ionisation energy for [NeII] only suffers a modest decrease. This shows that the virtual absence of [ArIII] and [NeII] lines after 6 Myr is due to the "absence" of hard enough continuum for these ion species.

---

[6] `http://web.pd.astro.it/panuzzo/hii/index.html`

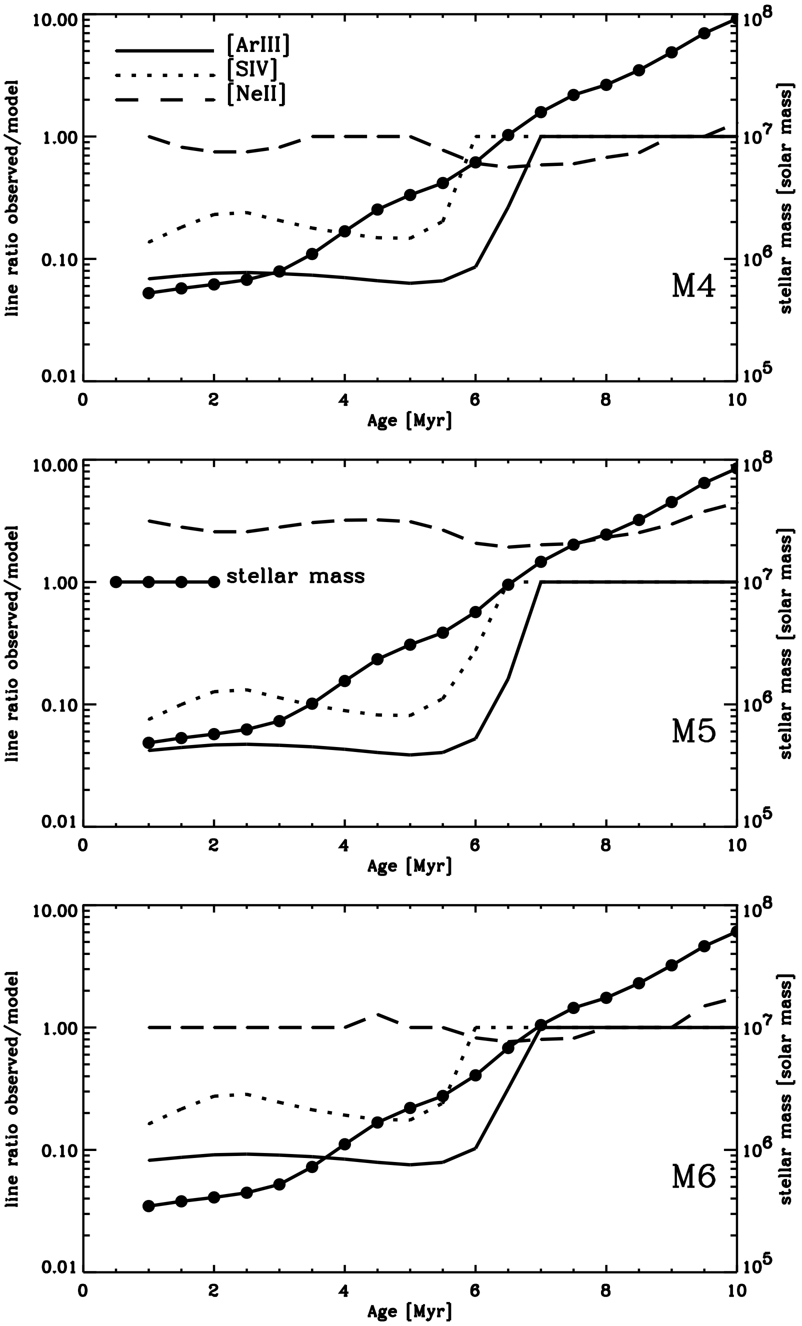

Fig. 16. For each cluster, and for the extinction derived in Sect. 4.1, this figure gives the ratios between observed and modelled [ArIII], [SIV] and [NeII] lines after correcting for the extinction correction and normalising the modelled Brγ fluxes to the observed ones. The ratio is set to one when the modelled flux is inside the error bar, or below the upper limit, which is the case for [ArIII] and [SIV]. The total stellar mass (taking into account evolutionary effects) is also plotted for each possible age.

The firm conclusion to be drawn from Fig. 16 is the strong evidence for the YMCs in NGC 1365 being older than 6 Myr. Because of the large amount of fading undergone by stellar clusters along the first Myr of their evolution, the fact that they are relatively old also implies that they are very massive. Let us consider the age of 7 Myr: the computed stellar masses in this case for M4, M5 and M6 are then 1.6, 1.5 and 1.0×10^7 $M_\odot$ for a 1 $M_\odot$ lower mass limit of the IMF.

We show in Fig. 18 the stellar mass function in M4 with these parameters (age of 7 Myr and mass of 1.6×10^7 $M_\odot$). The most massive stars in the clusters, 20−25 $M_\odot$, are several 10^4 in number, while low mass stars are expected to be present in millions.

Consideration of a line flux library with lower filling factors shows that, while the [ArIII] line flux is not affected, the [SIV] line flux may increase by a factor of up to 10. This remains consistent with the data as long as the clusters are only about 1 Myr older than the age derived for a filling factor of 10^{-3}. Hence, a safe range for the age of the YMCs is 6−8 Myr. We exclude the clusters being older than 8 Myr since if it was the case, the masses derived would be of the order of 10^8 $M_\odot$ for the only stellar component and become incompatible with the CO measurements by Sakamoto et al. (2007).

This is consistent with the detection of the CO absorption lines at 2.3 μm in the spectra of M4, M5 and M6, since this CO feature only appears after 6 Myr (Leitherer et al. 1999).

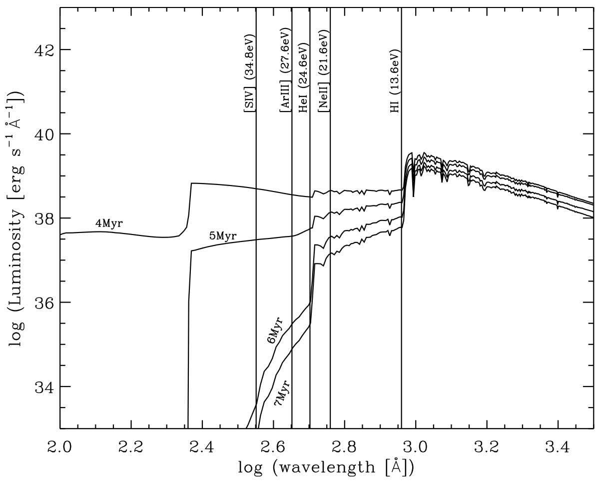

Fig. 17. Starburst99 model spectra for an instantaneously formed Salpeter cluster at ages 4, 5, 6 and 7 Myr. The vertical lines show the first ionisation potentials for H, [NeII], He, [ArIII] and [SIV].

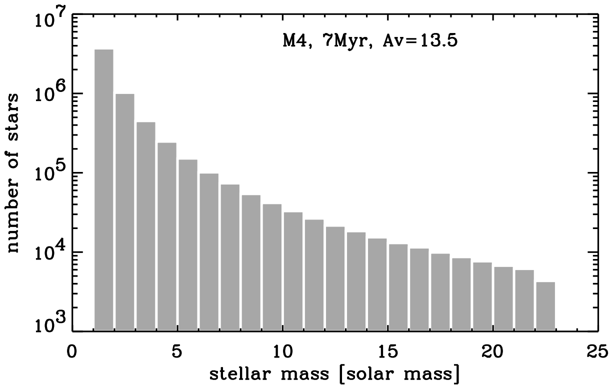

Fig. 18. Mass function for M4, given the age and mass derived in Sect. 4.2.

In principle, one could also use the ratio HeI 2.06 μm/Brγ to derive information about the hardness of the ionising continuum radiation, hence the age of the stellar population (Doyon et al. 1992). However, Shields (1993) and Lumsden et al. (2003) have demonstrated that the use of this ratio is not reliable.

4.3. Ionising photon emission rate

Using the NIR extinctions derived above, we can compute the de-reddened hydrogen line fluxes, and examine the ionising photon emission rates of the YMCs. For an ionisation-bound situation, justified for an embedded cluster, all the ionising photons ($\lambda \leq 912$ Å) emitted by the stars are absorbed. The number of H ionising photons is then directly proportional to the flux in any specific recombination line. From Osterbrock (1989):

$$Q[\mathrm{H}^+] = \frac{\alpha_\mathrm{B}}{\alpha^\mathrm{eff}_{\mathrm{H}\alpha}} \times \frac{L_{\mathrm{H}\alpha}}{h\nu_{\mathrm{H}\alpha}} \quad \text{, where } \alpha_\mathrm{B}/\alpha^\mathrm{eff}_{\mathrm{H}\alpha} \sim 2.96. \tag{1}$$

The Brγ de-reddened fluxes of M4, M5 and M6 being in the ranges [8.2–12.3], [7.6–11.5] and [13.7–20.6] $\times 10^{-15}$ erg s^{-1} cm^{-2}, leads to ionising photon emission rates in the ranges [3.4–5.1], [3.2–4.8] and [5.7–8.6] $\times 10^{52}$ s^{-1}.

Let us check now whether the ionising photon emission rates derived from the Brγ de-reddened fluxes of M4, M5 and M6 are consistent with the observed radio data in the centimetre range, given the ages just derived for M4, M5 and M6. The measurements reported in Table 1 and performed by Sandqvist et al. (1995) indicate negative indexes revealing, as expected for young clusters of the derived ages, the presence of a non-thermal component. The measurements also show that the indexes become increasingly positive with increasing wavelength ($\alpha^{20\,\mathrm{cm}}_{6\,\mathrm{cm}} > \alpha^{6\,\mathrm{cm}}_{2\,\mathrm{cm}}$). This is the signature of optically thick radio emission. Indeed, it is known that UDHII regions can be optically thick even at 6 cm (Kobulnicky & Johnson 1999). In Sandqvist et al. (1995), even though the 2 cm fluxes are not given explicitly, one can extrapolate their values using the 6 cm flux and the 6 cm/2 cm spectral indexes (given in their Table 2). The 2 cm flux is interesting, since it is both optically thin and likely to be free of any non-thermal contribution. Under this assumption, the measured radio fluxes provide independent estimates of the ionising photon emission rates of the clusters. From Table 2 from Sandqvist et al. (1995), we obtain the following 2 cm fluxes for M4, M5 and M6: 1.75 mJy, 0.61mJy, 1.70 mJy respectively. The corresponding figures for the ionising photon emission rates are 2.0×10^{52} s^{-1}, 7.0×10^{51} s^{-1} and 1.9×10^{52} s^{-1}. These values are slightly lower than, but in reasonable agreement with those derived from the de-reddened emission lines.

4.4. Final remarks about the derived YMC parameters

During this procedure, the derivation of the cluster mass and the derivation of the ionising photon emission rate depend on the validity of the assumption of a uniform foreground extinction. Conversely, the age derivation is quite robust and relies essentially on the disappearance of some emission lines relative to others. The factor to be matched is huge, one to two orders of magnitude, and can in no way be understood in terms of measurement uncertainties.

Would there be a way to explain the observed line ratios, maintaining a very young age (around 1 Myr)? Indeed, instead of the Salpeter IMF which we consider, we might invoke an ad-hoc IMF with a low upper cutoff (at about 23 $M_\odot$), but such a value is not justified. In addition, the observed negative spectral indexes of the radio emission from the YMCs constitute an independent argument favouring advanced ages, since the non-thermal component of the centimetre emission traces the presence of supernovae, which only occur after 3–4 Myr. Therefore, we retain our age determinations as providing the most reasonable interpretation.

For the quoted age range for the clusters (6–8 Myr), the corresponding stellar masses for the three clusters are in the range $[0.6\text{–}3.] \times 10^7\ M_\odot$. These masses are derived from the unextinguished Brγ fluxes and a Salpeter IMF with a lower boundary at 1 $M_\odot$. These masses must be multiplied by 2.5 if the lower boundary of the IMF is decreased to 0.1 Myr.

The uncertainty on the estimate of the dereddened line luminosities, which we recall is performed under the assumption of foreground extinction, is of the order of only 20%, hence small with respect to the uncertainty due to the uncertainties on the age and the IMF shape.

We hence conclude that the clusters are 6–8 Myr old, with masses of the order $10^7\ M_\odot$ and ionising photon emission rates of several 10^{52} s^{-1}.

All these elements suggest that the three MIR/radio sources in NGC 1365 are among the most massive clusters observed so far. Surprisingly for their relatively "advanced" age, their MIR emission indicates that they have not yet swept away all of their surrounding material. Usually, clusters are believed to very quickly remove the material in which they formed, within a few million years. The peculiar case of these YMCs raises the

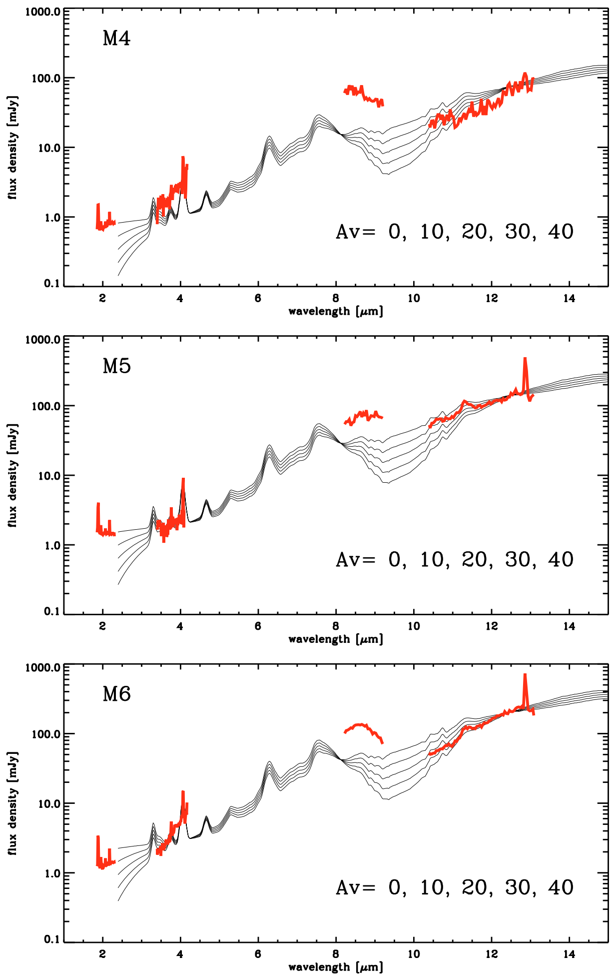

Fig. 19. Comparison between the observed spectra of NGC 1365/M4, M5 and M6 to the ISO CVF spectra of R136 suffering from distinct foreground extinctions, from $A_v = 0$ to $A_v = 40$. The CVF spectra are normalised to the VISIR spectra at 12.5 μm.

question of whether their extreme mass and their location close to the dust lane of their host galaxy play a role in the fact that, at 7 Myr, they still contain large amounts of gas.

5. Fitting the YMC NIR/MIR SEDs

In this section, we discuss the fitting of the NIR/MIR SED of the YMCs. We later add the constraints from their emission line spectrum.

5.1. Analysis of the NIR/MIR SEDs through comparison with R136

First, we examine in Fig. 19 a comparison of the SEDs of M4, M5 and M6 with the ISO CVF spectrum of R136, scaled to the distance of NGC 1365, normalised at 12.5 μm, and subject to some foreground extinction: we use a set of foreground extinctions in the range $A_\mathrm{v} = 0$ to $A_\mathrm{v} = 40$.

In the 8–9 μm window, the three NGC 1365 YMCs are brighter than R136 by factors between 2 and 10. This factor cannot be explained by a calibration error for the 8–9 μm range (see Sect. 2.4) since, in the worst case, we evaluated a flux uncertainty of a factor of 2 for this region of the spectrum. Even though a full N-band spectrum is needed to decisively settle this difference, the high 8–9 μm continuum may be due to the presence in the YMCs of a bright 8.6 μm PAH feature. In the usual PAH templates (as used in GRASIL, Silva et al. 1998), the 12.7 μm feature is much brighter than the 8.6 μm feature. However, the 8.6 μm feature can be significantly boosted for a high degree of ionisation of the PAH molecules. Indeed, for ionised PAHs, the ratio of cross sections $\sigma_{8.6}/\sigma_{12.7}$ is enhanced by a factor of 7–8 with respect to the neutral case (Li & Draine 2001; Draine & Li 2007).

In the 10–13 μm part of the SED, its slope can be reasonably matched by a foreground extinguished version of the R136 spectrum. In particular the 10 μm–13 μm VISIR spectra are well reproduced for M5 and M6 (including the 11.3 μm PAH feature). For M4, the resemblance is not so obvious, but the M4 SED is also noisier.

In summary, the SED of M5 resembles that of R136, except in the 8 μm–9 μm region where ionised PAH, boosting the 8.6 μm feature, could be an explanation. Therefore, M5 could be seen as a scaled-up version of R136, from the SED point of view. However, the emission line ratios discussed earlier clearly show that M5 cannot have the same age as R136, but is at a more advanced stage of 6–8 Myr. This is not a contradiction because the SED matching is not an age estimator. The key issue is to understand how M5, at 7 Myr, could have retained some dust component.

What is the conclusion of the comparison with R136 for M4 and M6? A very distinctive feature observed in M4 and M6 is their steep continuum rise between 3 μm and 4 μm, unlike the spectrum of R136. This type of feature is reminiscent of the emission from an optically thick dust component and suggests its presence in the YMCs. Therefore, we investigate hereafter such a possibility, using a more complex modelling tool.

5.2. Modelling of the NIR/MIR SEDs

Let us compare the SEDs we have in hand for the three YMCs to the SED prediction of a cluster including two components: (a) an optically thick component, which we will call the “molecular cloud” component, with stellar mass M_mc (which we would assume to be associated with the “youngest” stellar population in the cluster, if the star formation was not instantaneous) and (b) an optically thin component, which we will call the “cirrus” component, with a stellar mass M_cirrus (which we assume to be associated with the gas and with the “oldest” stellar population in the cluster).

We use `GRASIL` (Silva et al. 1998) to model the SED cluster. In a broad framework, `GRASIL` is designed to model the spectro-photometric evolution of dusty galaxies, including a detailed treatment of the radiative transfer through dust. It can be used to simulate the evolution of the properties and emission of a stellar population with the two components as described above: (a) the “molecular cloud component” for which the stars are still located at the centre of their parent molecular cloud and for which a large optical thickness is expected; and (b) the “cirrus component” in which both the stars and the dusty gas show an extended distribution, and for which the optical thickness is globally low.

Figure 20 illustrates how such a two-component model can match the global features of the observed SEDs of the three YMCs. This figure displays the observed SEDs for M4, M5 and M6 (in black). For each source, the R136 spectrum scaled at around 2 μm is superimposed (in brown). Also, the different components of the model are superimposed and shown with the following colour code: in green the joint stellar emission and continuum emission from the HII region arising from the

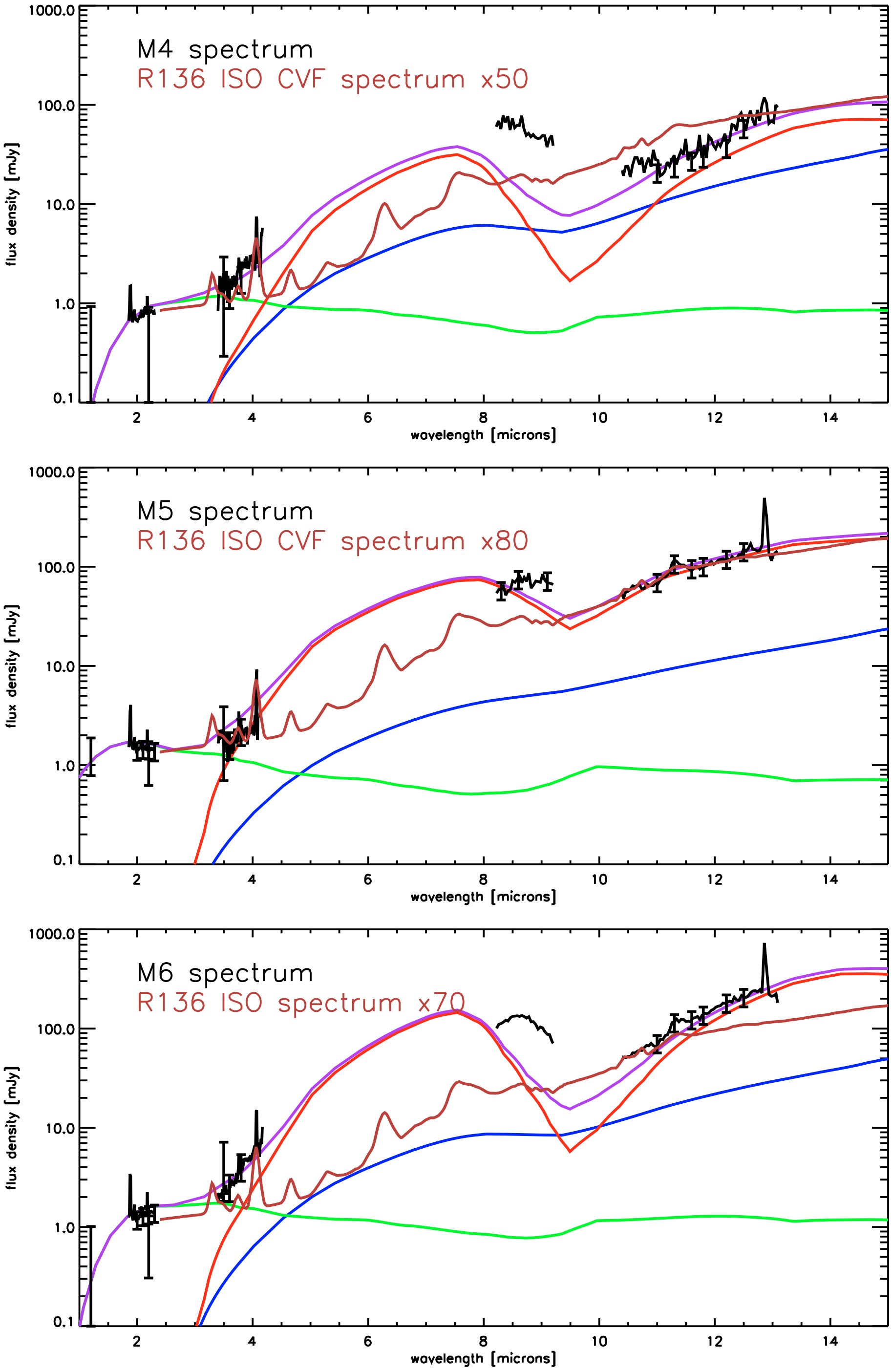

Fig. 20. Comparison of the observed spectra of M4, M5 and M6 (black) to the scaled ISO CVF spectrum of R136 (brown) and to the predicted spectra of the 2-component model described in the text. For the modelled spectra, the colour coding is the following: purple is the total spectrum (properly scaled for comparison with the source spectra); red is the total spectrum of the molecular cloud component (the optically thick one) component; blue is the spectrum of the dust (essentially very small grains, VSG) emission of the cirrus component (the optically thin one) and green is the spectrum of the [stellar+gas] component of the cirrus component.

"cirrus" component, in blue the dust emission from the "cirrus" component, in red the net emission from the thick "molecular cloud" component (dust and stellar emission, but essentially dominated by the dust) and in purple the total emission. The key parameter for the modelled "molecular cloud" component is its optical depth. For each YMC, this optical depth has been chosen in order to fit the slope in the red wing of the silicate feature around 10 μm, observed in the YMC, and has been derived after full treatment of the radiative transfer. The extinction values A_v which are required to reproduce the observed silicate feature red wing slopes are very large: respectively 100, 70 and 130, for M4, M5 and M6. Indeed, for the modelled "molecular cloud" component, dust is simultaneously the source of emission and extinction. For details about the radiative transfer in `GRASIL`, see Silva et al. (1998). Notice that the effect of such an extinction cannot be compared in a straightforward manner to the effect of the simple foreground extinction shown in Fig. 19 at the beginning of this section, and estimated by comparing the YMC SED to the R136 spectrum.

Following this modelling, the NIR 3−4 μm slope and the MIR slope between 10 μm and 13 μm are both steep as a result of the emission of the "molecular cloud" component and an important bump in the SED in the 4−8 μm range is predicted. This is consistent with the observed rise of the SED in the 3−4 μm range, in M4 and M6.

In conclusion, the NIR/MIR modelled SEDs in Fig. 20 provide qualitative matches for the observed SEDs in M4 and M6. In the case of M5, the slope of the continuum in the

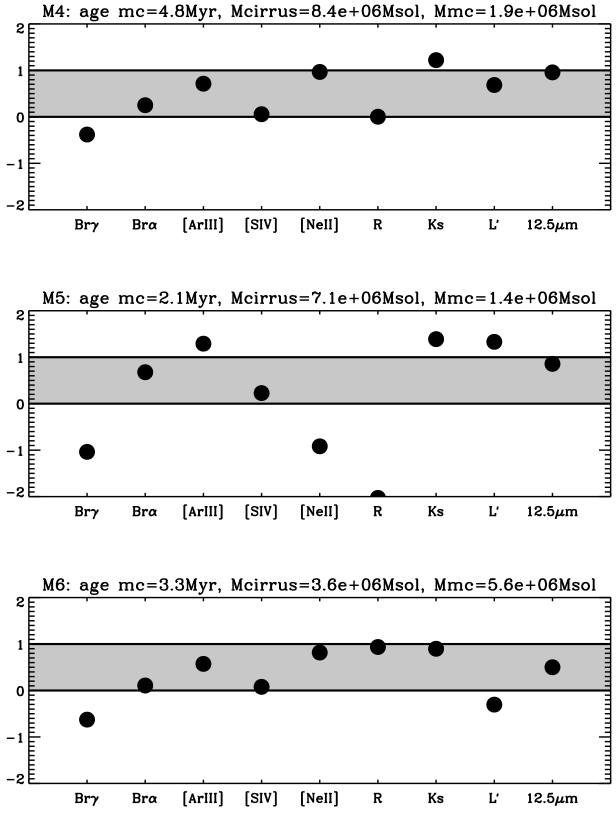

Fig. 21. Quality of the 9 predicted observables for the 2-component model for M4, M5 and M6 (see Sect. 5). The observed uncertainty is shown with the grey stripe. If $\mathrm{obs}_{\mathrm{min}}$ and $\mathrm{obs}_{\mathrm{max}}$ represent the *lower and upper limits* of the error bar, then the value on the Y-axis is $(\mathrm{mod} - \mathrm{obs}_{\mathrm{min}})/(\mathrm{obs}_{\mathrm{max}} - \mathrm{obs}_{\mathrm{min}})$, where mod is the predicted value. For the observables for which we only measure an upper limit, then a value $Y = 0$ is given to the corresponding point if the mode led value is lower than this limit.

NIR 3−4 μm range is overestimated in the model and the presence of a "molecular cloud" component does not seem to be mandatory.

Now we investigate the possibility that the "molecular cloud" component represents a second stellar generation (hence younger), still deeply embedded in dust. For this purpose, we perform fits of the two-component model predictions using the following observational constraints: the Brγ, Brα, [ArIII], [SIV] and [NeII] fluxes, and the R, Ks, L' and 12.5 μm flux densities. The age of the cirrus component is set to 7 Myr (derived earlier from the analysis of the line ratios) and the optical thickness of the "molecular cloud" component to the values given above and derived from the silicate red wing slope. The free parameters in the fits are the age and mass M_{mc} of the "molecular cloud" component (the age is forced to be ≤6 Myr), the mass M_{cirrus} of the "cirrus" component and the foreground extinction. Given the observational uncertainties and because the centre of the error-bar does not necessarily represent the most probable value of the observable, different solutions can be found. Yet, the results are globally identical. The quality of the fit for one solution is shown graphically in Figs. 21 and 20. For each observable, the error-bar has been scaled to the range [0−1]: the values of the modelled observables are given on the same scale. A dot inside the grey zone means that the modelled observable falls inside the error-bar.

The solutions shown in Fig. 21 are good for M4 and M6, and marginally acceptable for M5. Indeed, Fig. 20 already showed that the two-component model predicts a steep slope in the 3−4 μm range which is observed for M4 and M6, but not for M5. For the fits presented in Fig. 21, the age of the "molecular component", the stellar mass of the "cirrus" component and the stellar mass of the "molecular cloud" component are indicated above each plot. For M4, the stellar mass in the "molecular component" is four time lower than in the "cirrus" component. On the contrary, it is almost two times greater in the case of M6. Indeed, in Fig. 20 the relative importance of the "molecular component" (red) to the "cirrus component" (green and blue) is clearly greater in M6 than in M4.

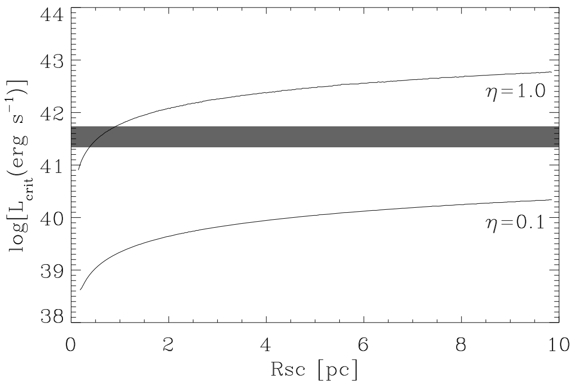

Fig. 22. Threshold mechanical luminosity for two heating efficiency (after Fig. 4b of Wünsch et al. 2007). The horizontal line shows that, according to our estimates, the three MIR/radio clusters of NGC 1365 lie in the bimodal regime region.

The two-component model presented here, even though simplifying a complex real situation and at the same time involving a large number of parameters, allows an interesting qualitative match to the observables. This is true to a good extent for M4 and M6. Notice that the two-component model predicts a bump in the SED in the 4−8 μm range, differing from the R136-type SED. The SED of M5, on the contrary, looks more like that of R136, and does not require the presence of a thick "molecular cloud" component. This might be related to the fact that M5 is seen lying slightly outside the dust lane, while M4 and M6 project in the dust lane. Indeed, the fact that the pressure of the surrounding interstellar medium is higher around M4 and M6 than around M5 may have affected their evolution and hence their intrinsic properties, and in peculiar their ability to remove the material from which they initially formed.

5.3. Conclusions on the YMC parameters

Let us summarise the conclusions reached after the successive steps of the data analysis.

First, we have found that the three YMCs in NGC 1365 are compact clusters. This is a solid conclusion, coming from a direct comparison with the cluster R136 in the LMC.

Second, the age estimates of the YMCs come from three independent channels:

(a) their NIR emission line ratios, with intense [NeII] and undetectable [ArIII] and [SIV] lines, can be understood only if their age is in the range 6−8 Myr;
(b) their radio indexes are steep, suggesting that the non-thermal contribution (supernovae remnants) is larger than the thermal contribution (HII region): although it is not possible to extract a precise value of the cluster age from its radio index, we know that the clusters must be older than 3 Myr;

(c) the detection of the CO absorption lines at 2.3 μm in their spectra tells us that the YMCs are older than 6 Myr.

Therefore, we find the YMC ages to be around 7 Myr. This again is a fairly solid conclusion.

Third, given their ages and their ionising photon emission rates (hence stellar luminosities), the stellar masses of the YMCs are found to be of the order of 10^7 $M_\odot$, implying a mass of the initial molecular material from which they formed of at least several 10^7 $M_\odot$. The molecular mass deduced from CO observations by Sakamoto et al. (2007), of the order of 10^9 $M_\odot$, is indeed consistent with the figure we have obtained.

Fourth, we find that, after 6 to 8 Myr of evolution, large amounts of gaseous/dusty material, traced by the radio/MIR emission and nebular lines, are still found within or in the vicinity of the star cluster. Since star clusters usually sweep away their gas on a much shorter time scale, our observations present a case for trapping of material in star clusters, at very high masses and in a dense environment. This gas trapping can lead to unusual evolution of the star clusters by allowing subsequent star formation events to happen.

In the following, we discuss, in the framework of the theoretical model by Tenorio-Tagle and co-workers, how such a gas trapping can be explained.

6. Gas trapping in the extremely massive clusters in NGC 1365

Theoretical work by the group of Silich and Tenorio-Tagle (Tenorio-Tagle et al. 2007; Wünsch et al. 2007; Silich et al. 2007) analyse in detail the hydrodynamics of the matter re-inserted in young clusters by stellar winds and supernovae ejecta. They show that in the case of massive and compact clusters, the re-inserted material is exposed to strong radiative cooling in the central parts of the clusters, because of the high density of the gas in these regions. This strongly affects the dynamics of the gas and can lead to a bi-modal hydrodynamic solution: (i)) the matter injected inside a certain radius called the *stagnation radius* is accumulated and eventually becomes gravitationally unstable leading to further star formation and; (ii)) outside the *stagnation radius*, the re-inserted material flows out of the cluster, building up a stationary wind (Wünsch et al. 2007).

One candidate for such a bi-modal gas behaviour has been identified in M82 by Silich et al. (2007), using observations from Smith et al. (2006). The observed parameters of the cluster, called M82-A1, imply such a bi-modal hydrodynamic solution. The adopted model leads to a much reduced rate of mass deposition in the interstellar matter, and a much reduced wind terminal velocity, compared to the adiabatic wind model.

The three clusters NGC 1365/M4, M5 and M6 are also excellent candidates for displaying such a bi-modal behaviour: they are both very massive and compact, hence the gas density in their central regions is high. Also, the fact that with an age of 7 Myr, these clusters have still retained an important amount of gas and dust, as shown by their MIR emission, suggests that the gas removal mechanism has not been efficient. Finally, the suspected "molecular cloud" component which we derive from the SED modelling of M4 and M6 – the two YMCs which project onto the galaxy dust lane – could trace on-going star forming events, consistant with the prediction from the bi-modal model. Nevertheless, in the case of M6, we find that $M_{\rm mc} > M_{\rm cirrus}$. This is incompatible with the idea that, for M6, the "molecular component" traces ongoing star formation involving only the material re-inserted by the "first" generation stars. The higher pressure of the dust lane gas in which these two clusters seem to be embedded could also have increased the efficiency of the recycling of the matter into new generations of stars.

In order to investigate quantitatively whether the MIR/radio emitting clusters in NGC 1365 are viable candidates for this special regime, we have used the results published in Wünsch et al. (2007). Simple analytic formulae are provided to test whether a cluster is undergoing such a bi-modal hydrodynamic solution, or if it only drives a stationary wind. Figure 4 in Wünsch et al. (2007) displays the threshold mechanical luminosity as a function of the star cluster radius that separates a single stationary wind solution from bi-modal solutions. The threshold is shown to depend on the heating efficiency (parameter η in their work). This parameter represents the efficiency of the thermalization of the gas.

To estimate the mechanical luminosity of the clusters, we use the Starburst99 models (Leitherer et al. 1999): for a Salpeter 10^7 $M_\odot$ model, with solar metallicity, for an age range between 5 and 9 Myr, the range of mechanical luminosities is $10^{41.3}$ to $10^{42.7}$ erg s^{-1}. The radii of the cluster stellar component are smaller than 10 pc. This radius is directly measured for M5, and assumed for M4 and M6, where no clear visible counterpart is detected. In the radius vs. luminosity diagram of Wünsch et al. (2007), reproduced in Fig. 22, the clusters clearly fall in the bi-modal solution region.

The picture drawn here of the three bright MIR/radio sources seems coherent. In the massive reservoir of matter surrounding the nucleus of NGC 1365, and shown by the prominent dust lane, very massive and compact clusters have formed. The hydrodynamics of the gas inside these clusters (re-inserted and/or unused for star formation) tends to follow the bi-modal hydrodynamic solution described above. This leads to a much less efficient removal of the gas, which stagnates in the inner regions of the clusters, while it is ejected in the outer regions with reduced velocities compared to common adiabatic cluster outflows. This could be traced by the velocity gradient shown in Fig. 9, but we leave this analysis for a future publication.

7. Conclusion

The three MIR/radio sources in the circumnuclear star forming ring in NGC 1365 have been found to be very compact and very bright embedded clusters. Under the simple assumption of foreground extinction, their MIR emission line spectrum points towards ages of about 7 Myr. Such an age is also consistent with other age indicators like the slope of their radio centimetre emission or the CO absorption feature in their NIR spectrum. Given their ionising photon emission rate and age, these YMCs are found to be extremely massive objects, with a mass of at least 10^7 $M_\odot$. They are the most massive star clusters found so far. They must have formed from molecular clouds of several 10^7 $M_\odot$. This figure is consistent with the presence within the NGC 1365 central 2 kpc diameter region, where they are found, of large amounts of molecular gas, of the order of 10^9 $M_\odot$, as derived from the CO molecule emission.

The remarkable result of our analysis is the fact that such embedded YMCs have retained a large amount of gas and dust, in spite of their relatively advanced age, around 7 Myr. This puzzling fact may be related to the extremely high mass of these three YMCS. Indeed, some theoretical works have analysed the fate of re-injected gas in very massive clusters and found that the gas may be trapped and even lead to secondary star forming events. The three MIR/radio clusters in NGC 1365 are good candidates to test the predictions of such models.

Acknowledgements. We thank the daytime and nighttime support staff at Cerro Paranal Observatory, who made these observations possible, and the anonymous referee for her/his useful comments. E.G. thanks the ESO fellowship program and the PCI program of ON/MCT (DTI/CNPq grant number 383076/07-2).

References

Barth, A. J., Ho, L. C., Filippenko, A. V., & Sargent, W. L. 1995, AJ, 110, 1009
Beck, S. C., Turner, J. L., Langland-Shula, L. E., et al. 2002, AJ, 124, 2516
Benedict, G. F., Higdon, J. L., Jefferys, W. H., et al. 1993, AJ, 105, 1369
Boulanger, F., & Rubio, M. 2006, in Rev. Mex. Astron. Astrofis. Conf. Ser., 26, 5
Bower, G. A., & Wilson, A. S. 1995, ApJS, 99, 543
Conti, P. S., & Vacca, W. D. 1994, ApJ, 423, L97
Dors, Jr., O. L., & Copetti, M. V. F. 2005, A&A, 437, 837
Doyon, R., Puxley, P. J., & Joseph, R. D. 1992, ApJ, 397, 117
Draine, B. T., & Lee, H. M. 1984, ApJ, 285, 89
Draine, B. T., & Li, A. 2007, ApJ, 657, 810
Forbes, D. A., & Norris, R. P. 1998, MNRAS, 300, 757
Galliano, E., & Alloin, D. 2008, ArXiv e-prints, 805
Galliano, E., Alloin, D., Pantin, E., Lagage, P. O., & Marco, O. 2005, A&A, 438, 803
Gilbert, A. M., Graham, J. R., McLean, I. S., et al. 2000, ApJ, 533, L57
Gorjian, V. 1996, AJ, 112, 1886
Gorjian, V., Turner, J. L., & Beck, S. C. 2001, ApJ, 554, L29
Granato, G. L., Danese, L., & Franceschini, A. 1997, ApJ, 486, 147
Holtzman, J. A., Faber, S. M., Shaya, E. J., et al. 1992, AJ, 103, 691
Hunter, D. A., O'Connell, R. W., & Gallagher, III, J. S. 1994, AJ, 108, 84
Johnson, K. E. 2004, in The Formation and Evolution of Massive Young Star Clusters, ed. H. J. G. L. M. Lamers, L. J. Smith, & A. Nota, ASP Conf. Ser., 322, 339
Kobulnicky, H. A., & Johnson, K. E. 1999, ApJ, 527, 154
Larsen, S. S. 2004, ArXiv Astrophysics e-prints
Leitherer, C., Vacca, W. D., Conti, P. S., et al. 1996, ApJ, 465, 717
Leitherer, C., Schaerer, D., Goldader, J. D., et al. 1999, ApJS, 123, 3
Li, A., & Draine, B. T. 2001, ApJ, 554, 778
Lindblad, P. O. 1999, A&AR, 9, 221
Lumsden, S. L., Puxley, P. J., Hoare, M. G., Moore, T. J. T., & Ridge, N. A. 2003, MNRAS, 340, 799
Maoz, D., Barth, A. J., Sternberg, A., et al. 1996, AJ, 111, 2248
Martín-Hernández, N. L., Schaerer, D., & Sauvage, M. 2005, A&A, 429, 449
Meurer, G. R. 1995, Nature, 375, 742
Mirabel, I. F., Vigroux, L., Charmandaris, V., et al. 1998, A&A, 333, L1
Morganti, R., Tsvetanov, Z. I., Gallimore, J., & Allen, M. G. 1999, A&AS, 137, 457
Murtagh, F., & Starck, J.-L. 1999, Am. Astron. Soc. Meet., 194, 0
O'Connell, R. W., Gallagher, III, J. S., & Hunter, D. A. 1994, ApJ, 433, 65
O'Connell, R. W., Gallagher, III, J. S., Hunter, D. A., & Colley, W. N. 1995, ApJ, 446, L1
Osterbrock, D. E. 1989, Astrophysics of gaseous nebulae and active galactic nuclei, Research supported by the University of California, John Simon Guggenheim Memorial Foundation, University of Minnesota (Mill Valley, CA: University Science Books), 422
Panuzzo, P., Bressan, A., Granato, G. L., Silva, L., & Danese, L. 2003, A&A, 409, 99
Plante, S., & Sauvage, M. 2002, AJ, 124, 1995
Sakamoto, K., Ho, P. T. P., Mao, R.-Q., Matsushita, S., & Peck, A. B. 2007, ApJ, 654, 782
Sandqvist, A., Joersaeter, S., & Lindblad, P. O. 1995, A&A, 295, 585
Shaya, E. J., Dowling, D. M., Currie, D. G., Faber, S. M., & Groth, E. J. 1994, AJ, 107, 1675
Shields, J. C. 1993, ApJ, 419, 181
Silich, S., Tenorio-Tagle, G., & Muñoz-Tuñón, C. 2007, ApJ, 669, 952
Silva, L., Granato, G. L., Bressan, A., & Danese, L. 1998, ApJ, 509, 103
Smith, L. J., Westmoquette, M. S., Gallagher, J. S., et al. 2006, MNRAS, 370, 513
Tenorio-Tagle, G., Wünsch, R., Silich, S., & Palouš, J. 2007, ApJ, 658, 1196
Whitmore, B. C., & Schweizer, F. 1995, AJ, 109, 960
Whitmore, B. C., Schweizer, F., Leitherer, C., Borne, K., & Robert, C. 1993, AJ, 106, 1354
Wold, M., & Galliano, E. 2006, MNRAS, 369, L47
Wünsch, R., Silich, S., Palouš, J., & Tenorio-Tagle, G. 2007, A&A, 471, 579